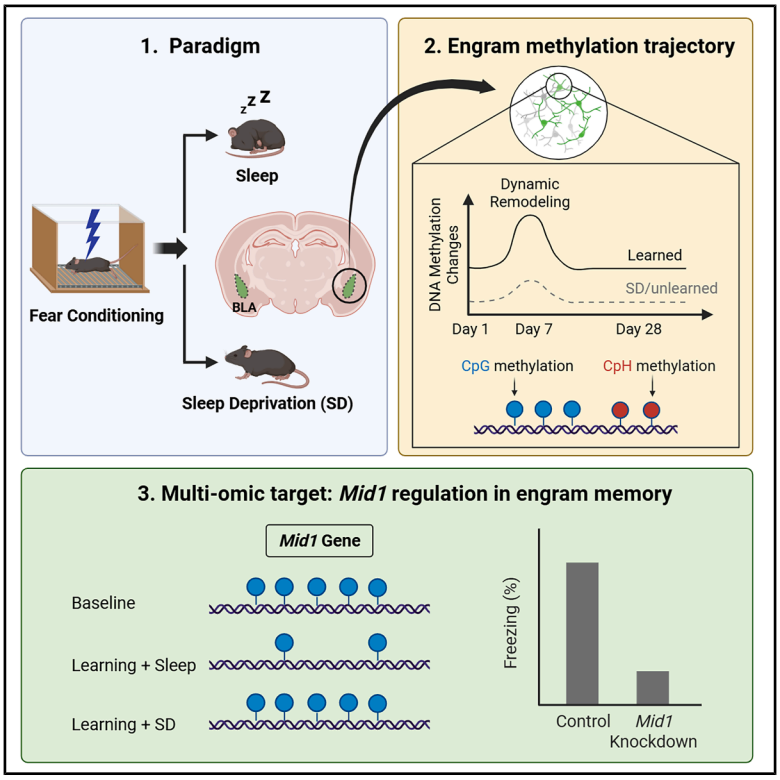
Cell Reports

Article

Sleep-dependent DNA methylation remodeling in basolateral amygdala fear engrams

Graphical abstract



Authors

Xinyue Chen, Fanwei Ruan, Angie Maldonado Rodriguez, ..., Wanding Zhou, Yueqing Peng, X. Shawn Liu

Correspondence

yp2249@cumc.columbia.edu (Y.P.), sl4738@cumc.columbia.edu (X.S.L.)

In brief

Chen et al. show that DNA methylation in memory-encoding neurons changes over weeks following learning. Sleep deprivation disrupts these changes, reducing neuronal recruitment into the memory trace and impairing memory. They identify *Mid1* as a methylation-regulated gene required for fear memory, linking epigenetic remodeling, sleep, and memory storage together.

Highlights

- Dnmt-mediated DNA methylation in BLA is required for learning and memory
- Learning induces dynamic CpG and CpH DNA methylation changes in BLA fear engrams
- Sleep deprivation impairs learning-induced methylation changes in BLA engrams
- Methylome-transcriptome integration identifies *Mid1* as required for fear memory

Chen et al., 2026, Cell Reports *45*, 118190
November 24, 2026 © 2026 The Authors. Published by Elsevier Inc.
https://doi.org/10.1016/j.celrep.2026.118190

CellPress

Cell Reports

CellPress
OPEN ACCESS

Article

Sleep-dependent DNA methylation remodeling in basolateral amygdala fear engrams

Xinyue Chen,[1,2,4] Fanwei Ruan,[3,4] Angie Maldonado Rodriguez,[2] Richard Pan,[4] Ruizhi Wang,[2] Michelle Jin,[1,6] Lianyan Zhou,[2] Kehan Yi,[4] Hanqing Liu,[7] Wanding Zhou,[8,9] Yueqing Peng,[2,5,*] and X. Shawn Liu[4,10,*]

[1]Department of Neuroscience, Vagelos College of Physicians and Surgeons, Columbia University Medical Center, Columbia University, New York, NY 10032, USA
[2]Department of Neurology, Vagelos College of Physicians and Surgeons, Columbia University, New York, NY 10032, USA
[3]Graduate Program in Quantitative and Computational Biosciences, Baylor College of Medicine, Houston, TX 77030, USA
[4]Department of Physiology and Cellular Biophysics, Vagelos College of Physicians and Surgeons, Columbia University Medical Center, Columbia University, New York, NY 10032, USA
[5]Department of Pathology and Cell Biology, Vagelos College of Physicians and Surgeons, Columbia University Medical Center, Columbia University, New York, NY 10032, USA
[6]Department of Psychiatry, Vagelos College of Physicians and Surgeons, Columbia University, New York, NY 10032, USA
[7]Department of Neurobiology, Harvard Medical School, Boston, MA 02115, USA
[8]Center for Computational and Genomic Medicine, The Children's Hospital of Philadelphia, Philadelphia, PA 19104, USA
[9]Department of Pathology and Laboratory Medicine, University of Pennsylvania, Philadelphia, PA 19104, USA
[10]Lead contact
*Correspondence: yp2249@cumc.columbia.edu (Y.P.), sl4738@cumc.columbia.edu (X.S.L.)
https://doi.org/10.1016/j.celrep.2026.118190

SUMMARY

How sleep consolidates fear memories at the molecular level within individual engram neurons is unknown. Using activity-dependent tagging and sequencing, we profiled the DNA methylome and transcriptome of engram and non-engram nuclei from the basolateral amygdala (BLA) after contextual fear conditioning with and without post-learning sleep deprivation. Fear learning induces coordinated CpG and CpH DNA methylation remodeling specifically in engram neurons, with each showing unique temporal dynamics, revealing CpH methylation as a separate component of the engram's epigenetic signature. Interestingly, sleep deprivation partially reverses learning-induced methylation changes and impairs memory recall, indicating that sleep supports engram-specific epigenetic consolidation. Integrating the engram methylome with single-cell transcriptome profiling, we construct a multi-omic molecular atlas of the BLA fear engram and identify *Mid1* as a learning- and sleep-regulated methylation target. BLA-wide and engram-specific *Mid1* knockdown establishes its functional requirement for fear memory consolidation, providing an approach to identify behaviorally relevant epigenetic targets.

INTRODUCTION

The formation of a long-term memory starts with acquisition, followed by consolidation, and eventual storage to enable retrieval when needed.[1] During the process of consolidation, sleep plays an essential role.[2–5] However, the underlying cellular and molecular mechanisms of how sleep consolidates memory are largely unclear.

At the cellular level, memory is thought to be encoded in specific neuronal ensembles, termed engrams, which are a subset of neurons sparsely distributed in the brain. These neurons are activated by learning, undergo biophysical and biochemical changes, and become necessary and sufficient for memory retrieval.[6–10] In a classical fear conditioning paradigm, engrams were demonstrated to exist in the hippocampus, cortex, amygdala, and other regions.[7,11–16] Among these regions, the basolateral amygdala complex (BLA) is a critical substrate for fear memory and a primary locus of dysregulation in post-traumatic stress disorder (PTSD) and anxiety disorders.[15,17–20] A recent study shows that stress can directly disrupt the engram ensemble in the lateral amygdala, a subnucleus of the BLA complex, leading to overgeneralization of fear, which provides mechanistic insights into fear-related pathology such as PTSD.[20] Moreover, transcriptomic analyses revealed that distinct populations within the BLA, including *Rspo2*/*Sema3e*-positive neurons, are associated with aversive behaviors.[21–23] However, whether and how BLA engrams participate in sleep-dependent memory consolidation, and what molecular mechanisms are engaged during this process, remain unknown.

At the molecular level, epigenetic modifications including DNA methylation, histone modification, 3D structure of chromatin,

This is an open access article under the CC BY-NC license (http://creativecommons.org/licenses/by-nc/4.0/).

and non-coding RNAs have been implicated in memory processings.[24–30] DNA methylation emerged as a compelling candidate substrate for engrams due to its biochemical stability in the otherwise dynamic neuronal environment, and its theoretical capacity to encode experience-dependent changes in a persistent yet flexible way.[31–36] This dynamic regulation is mediated by DNA methyltransferases (DNMTs), including the *de novo* enzyme DNMT3a and maintenance enzyme DNMT1, which catalyze the addition of methyl groups,[37] as well as ten-eleven translocation (TET) enzymes TET1, TET2, and TET3, which initiate active DNA demethylation in post-mitotic neurons.[38] Previous studies on these enzymes mainly focused on the hippocampus and cortex to show their involvement in synaptic plasticity, neuronal excitability, and memory.[39–44] However, DNA methylation in the BLA remains largely unexplored. Importantly, prior DNA methylation studies in the context of memory lack engram-level resolution,[34,36,45,46] except one single engram-specific study reporting CpG methylation exclusively.[47] Whether DNA methylation, particularly the neuron-specific non-CpG (CpH) methylation,[48,49] is dynamically regulated within engram populations and contributes to engrams in the BLA, remains an open question.

Here, we use activity-dependent tagging of BLA engram neurons combined with whole-genome bisulfite sequencing (WGBS) and single-nucleus transcriptome profiling (PIP-seq) to characterize the genome-wide DNA methylation and transcription landscapes of fear memory engram cells, revealing distinct remodeling of CpG and CpH methylation throughout one month after learning. We further demonstrate that post-learning sleep deprivation reduces BLA engram recruitment and interferes with learning-induced methylation changes to impair fear memory, linking post-learning sleep to engram-specific epigenetic remodeling. Integrating the engram methylome with single-nucleus transcriptomics, we identify *Mid1* as a learning- and sleep-regulated methylation target and demonstrate its requirement for fear memory through both BLA-wide and engram-specific manipulations.

RESULTS

Dnmt in the BLA is essential for fear memory

To confirm the essential role of DNA methyltransferases in fear memory, we crossed the activity-dependent genetic labeling TRAP2 mice[13] with Cre recombinase-induced *Dnmt3a* knockout mice[50] to enable deletion of *Dnmt3a* in neurons labeled during learning, hereafter referred to as putative engram cells. We administered 4-hydroxytamoxifen (4-OHT) upon fear learning to TRAP2$^{+/-}$;*Dnmt3a*$^{fl/fl}$(knockout) and TRAP2$^{-/-}$;*Dnmt3a*$^{fl/fl}$ (control) mice to delete *Dnmt3a*, then assessed memory performance. The efficacy of *Dnmt3a* knockout was validated by genotyping and immunostaining (Figures S1A–S1D). While both groups showed equivalent learning during initial acquisition, *Dnmt3a* knockout mice exhibited moderately but significantly impaired contextual and auditory fear memory retrieval at one week; contextual impairment persisted to one month, whereas auditory memory did not differ at that timepoint (Figures S1E–S1J), indicating that *Dnmt3a* is required for fear memory. These moderate impairments of fear memory are likely due to the complementary function of other Dnmt enzymes upon *Dnmt3a* deletion.[43]

To further investigate the function of DNA methylation enzymes in the BLA, we performed immunofluorescence (IF) staining of DNMT3A in the BLA of mice upon contextual fear conditioning (cFC). Compared to control mice (context-only with no shock), those with shock exhibited an increase of DNMT3A protein in the BLA (Figures 1A and 1B). Given the moderate memory impairments after *Dnmt3a* deletion (Figure S1), we reasoned that *Dnmt1*, the DNA methylation maintenance enzyme, may play a complementary role to *Dnmt3a* in learning and memory as reported.[43] Thus, we designed experiments to knockdown both *Dnmt3a* and *Dnmt1* by shRNA to assess their function in the BLA for learning and memory. As illustrated in Figure 1C, we stereotaxically delivered AAV-shRNAs targeting *Dnmt3a* and *Dnmt1* into the BLA and examined its impact on fear learning and memory at different time points. The knockdown efficacy for both enzymes was validated by RNA-seq (Figure S2A) and IF staining (Figure S2B). In Experiment i, we trained the animals two weeks after AAV-shRNAs injection, allowing sufficient time for AAV-mediated knockdown prior to learning. We observed dramatic impairments in learning and subsequent memory retrieval in the knockdown group, compared to the scrambled control group (Figures 1D–1F). In Experiment ii, we specifically examined the role of *Dnmt3a* and *Dnmt1* for memory and thus performed fear conditioning 3 days after AAV-shRNAs injection to ensure proper training. As expected, these animals showed normal learning patterns (Figure 1G). Strikingly, they still displayed robust impairment of memory retrieval (Figures 1H and 1I). The results from these two experiments indicate that *Dnmt3a* and *Dnmt1* are required for fear learning and memory in the BLA. In addition, we confirmed these shRNA knockdowns did not affect the anxiety or locomotion phenotypes, as examined via the open field test (Figures S2C–S2J), supporting the importance of *Dnmt3a* and *Dnmt1* in the BLA for learning and memory.

Learning induces dynamic and distinct CpG and CpH methylation changes in the BLA engrams

To investigate the function of DNA methylation enzymes, we examined whether learning induces DNA methylation changes in the BLA putative engram cells. We crossed TRAP2 mice with Sun1-GFP transgenic mice to selectively label these cells activated during contextual fear conditioning (cFC). Animals with cells activated by context-only without shocks (noFC) served as a control. One week (day 7) and one month (day 28) after cFC, we conducted a contextual fear recall test to confirm fear memory formation/retention, and immediately isolated the GFP+ and GFP- nuclei from the BLA of FC and noFC mice (schematic see Figure 2A; sorting strategy see Figures 2B and S7A), and performed Whole Genome Bisulfite Sequencing (WGBS). We generated single base-resolution DNA methylation maps for each experimental group. Each sample achieved a minimum of ~18X genome-wide (average ~42× across all samples), ensuring confident methylation quantification at individual cytosines and robust detection of differentially methylated regions (DMRs) across groups (Figure S3A; Table S1). While the overall methylation levels are similar among these samples

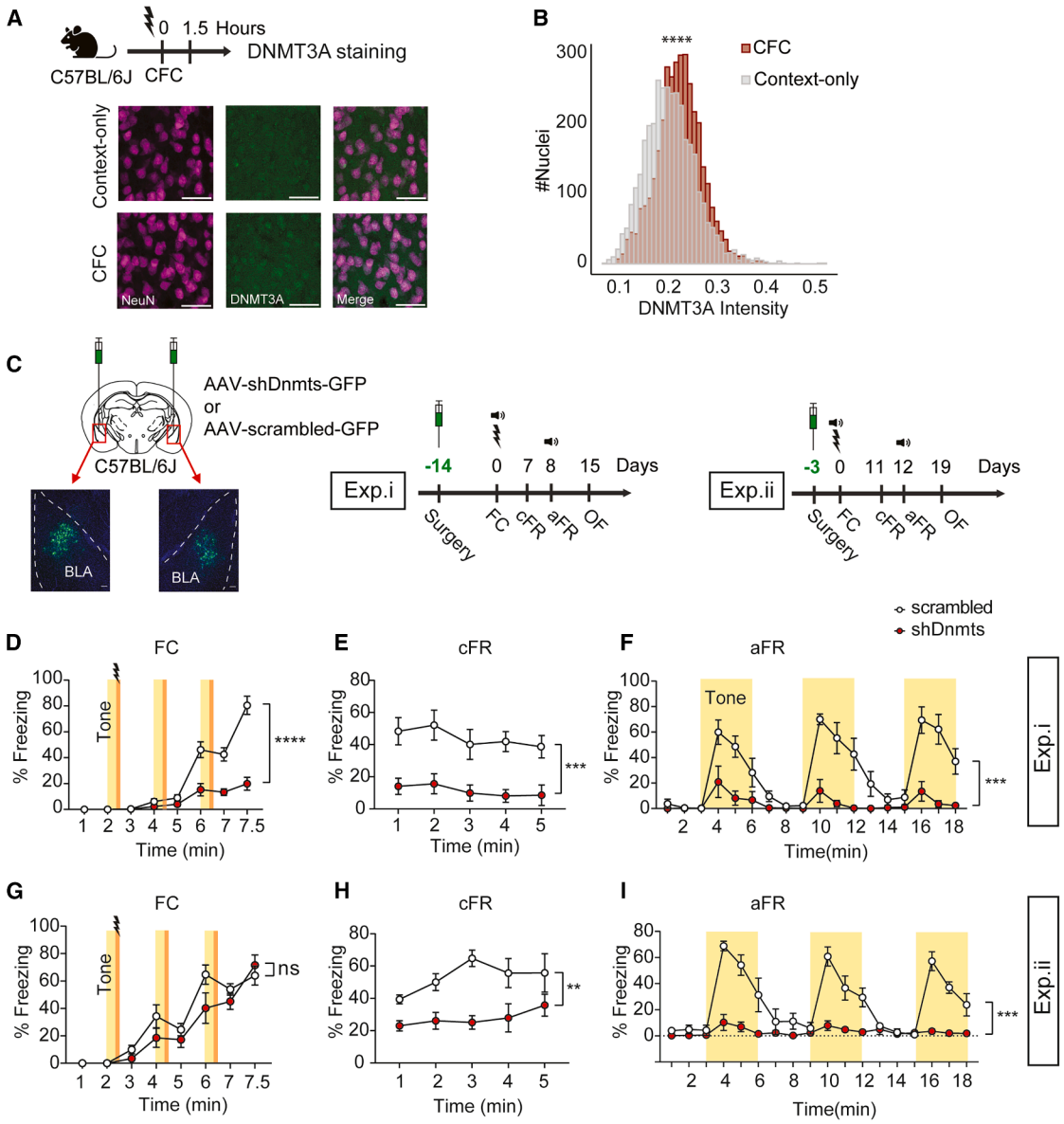


Figure 1. *Dnmt3a* and *Dnmt1* in the BLA are required for learning and memory

(A) Immunostaining of NeuN and DNMT3A 1.5 h after contextual fear conditioning (cFC). Scale bars, 50 μm.

(B) Histogram of DNMT3A intensity in cFC versus context-only mice. Unpaired two-tailed Kolmogorov-Smirnov test, $p < 0.0001$; $n = 3$ mice per group (context-only, 3,500 cells; cFC, 3558 cells).

(C) Left, schematic of AAV injection and expression of shRNAs targeting *Dnmt3a* and *Dnmt1* in bilateral BLA. Scale bars, 100 μm. Middle and Right, schematic of the experimental design in Experiment i (FC training 2 weeks after AAV injection) and Experiment ii (FC training 3 days after AAV injection).

(D) Freezing behavior during auditory fear conditioning (aFC) in Exp i. Shaded bars indicate tones (yellow) and foot shocks (orange) (two-way repeated measures (RM) ANOVA: treatment, F (1, 12) = 34.56, $p < 0.0001$; $n = 7$ per group).

(E) Freezing behavior during contextual fear recall (cFR) test on day 7 in Exp i (two-way RM ANOVA: treatment, $F_{1,12} = 21.82$, $p = 0.0005$).

(F) Freezing behavior during auditory fear recall (aFR) test on day 8 in Exp i. Percentage of freezing behavior was measured across an 18-min testing period. (Two-way RM ANOVA: treatment, $F_{1,12} = 20.51$, $p = 0.0007$; $n = 6$ per group).

(G) Freezing behavior during aFC in Exp ii (two-way RM ANOVA: treatment, $F_{1,10} = 1.963$, $p = 0.1915$).

(H) Freezing behavior during cFR test on Day 11 in Exp ii (two-way RM ANOVA: treatment, $F_{1,10} = 14.51$, $p = 0.0034$).

(I) Freezing behavior during aFR test on Day 12 in Exp ii (two-way RM ANOVA: treatment, $F_{1,10} = 32.45$, $p = 0.0002$). Data are shown as mean ± SEM. $^{*}p < 0.05$, $^{**}p < 0.01$, $^{***}p < 0.001$, and $^{****}p < 0.0001$; ns, not significant.

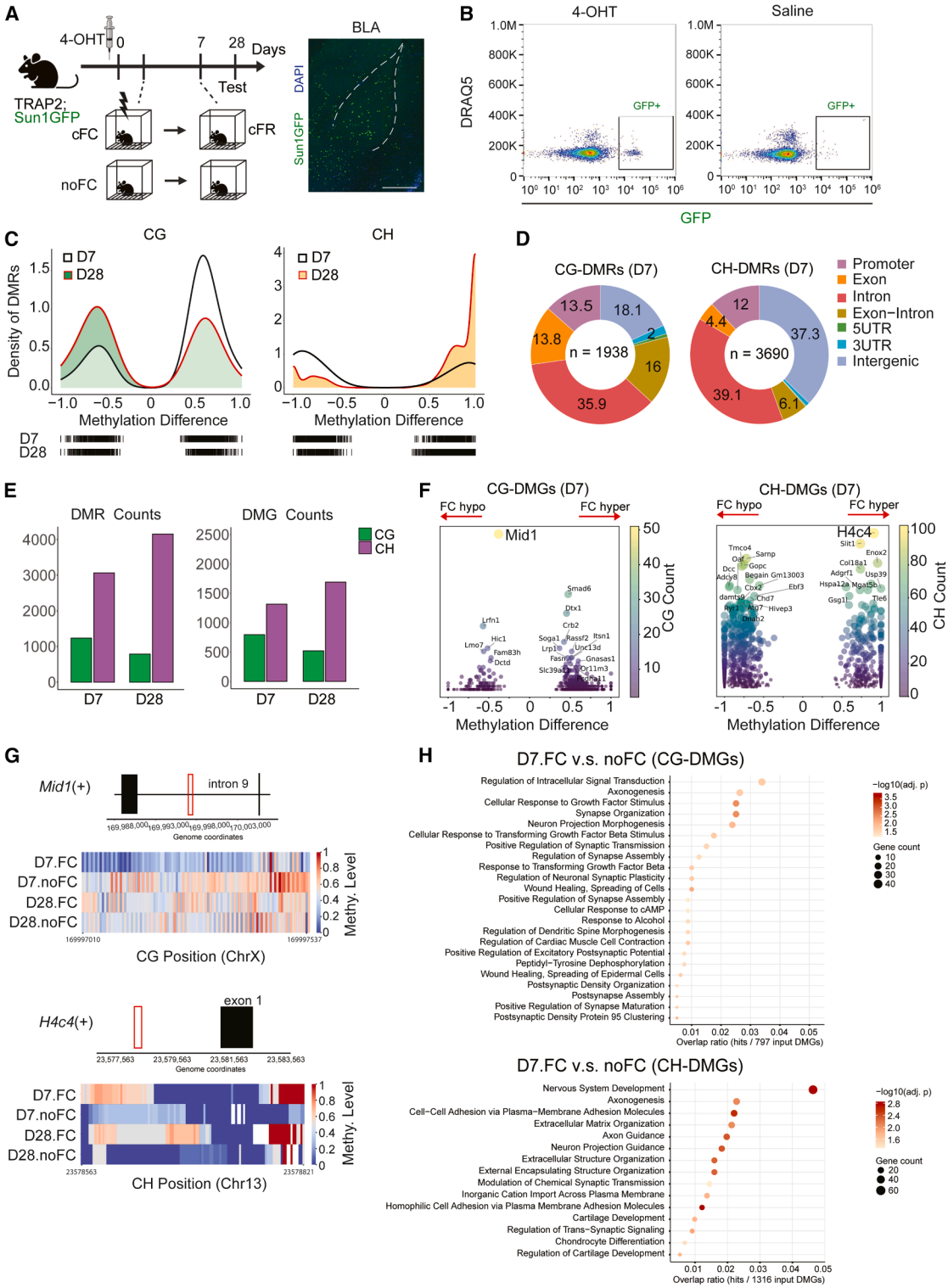


Figure 2. Learning induces dynamic methylation changes in BLA ensembles

(A) Left, Schematic of experimental design for WGBS. TRAP2; Sun1-GFP mice were injected with 4-hydroxytamoxifen (4-OHT) at 9:00 (ZT2). CFC or no-CFC (context exposure without shock) occurred at 14:00 (ZT7). On day 7 or day 28, immediately after contextual fear recall (cFR), BLAs were extracted from these mice for WGBS, $n = 2$ per group. Right, fluorescence image displaying labeled TRAPed GFP+ cells in the BLA. Scale bars, 500 μm.

(B) Representative FANS flow cytometry plots showing GFP+ cells in mice injected with 4-OHT and saline; y axis is the nuclear indicator DRAQ5.

(legend continued on next page)

(Figures S3B–S3C), we identified hundreds to thousands of DMRs in the context of CpG and CpH (H as A, C, or T) dinucleotide contexts (Figure 2E, left image) on Day 7 and Day 28.

To examine the dynamics of methylation changes after FC, we used density plots to visualize the DMR global patterns in both CG and CH contexts. On day 7, learning predominantly induced genome-wide hypermethylation in the CG context, with a peak around a 60% increase in methylation (methylation difference ≈ +0.6). In contrast, CH-DMRs on day 7 showed a strong bias toward hypomethylation, with more changes reflecting an 80–100% reduction in methylation (methylation difference ≈ −0.8 to −1.0). Interestingly, by day 28, the pattern in the CG context shifted toward hypomethylation, with a peak around −0.6, whereas CH-DMRs showed a broader distribution skewed toward hypermethylation (Figure 2C). This result indicates fear learning induces dynamic and distinct changes in canonical CG methylation and neuron-specific CH methylation throughout the month after learning.

Then we examined the genomic distribution of CG- and CH-DMRs. As shown in Figure 2D, CG-DMRs on day 7 were located mainly in introns (35.9%), followed by intergenic regions (18.1%), exon-intron boundaries (16%), exons (13.8%), and promoters (13.5%). Though CH-DMRs also showed a similar enrichment in introns (39.1%) and promoters (12%), they were more frequent in intergenic regions (37.3%), and less frequent in exon-intron boundaries (6.1%) and exons (4.4%). The CG- and CH-DMRs induced by FC on day 28 showed a similar pattern (Figure S4A). Since introns comprise a large portion of gene bodies, CG- and CH-DMRs are more likely to overlap introns simply by chance. To control this, we generated candidate randomized null DMRs preserving chromosome-level properties (DMR sizes, DMR number, DMR chromosomal distribution, GC content, CpG density, and gene density) and calculated the enrichment by comparing the observed annotation counts to those from the randomized null counts. We observed that CG-DMRs were mostly enriched in CpG islands as expected (Figure S4B). For example, the gene *Plpp1*, which encodes phospholipid phosphatase 1, contains a learning-induced CG-DMR at its first intron CpG island on day 7 that is lost by day 28 (Figure S4D). CG-DMRs were also enriched in enhancers on day 7, but not day 28 (Figures S4B and S4C). For instance, *Map3k14*, a serine/threonine protein kinase, similarly lost its learning-induced enhancer CG-DMR by day 28 (Figure S4E). In contrast, both CG- and CH-DMRs were consistently depleted from gene bodies (Figures S4B and S4C), suggesting that transcribed regions are relatively protected from learning-induced DNA methylation remodeling, with changes instead concentrated at *cis*-regulatory elements such as enhancers and CpG islands. Together, these analyses reveal a dynamic redistribution of DNA methylation at regulatory elements in BLA putative engram cells following fear conditioning.

To study the genes associated with DMRs, namely DMGs (differentially methylated genes), we categorized them into hypermethylation (methylation difference > 0.3; p value cutoff = 0.05) and hypomethylation (methylation difference < 0.3; p value cutoff = 0.05) in reference to noFC control group (Figure 2E right image and 2F). We ranked these DMGs based on the density of differentially methylated cytosines, prioritizing genes with larger, denser DMRs, which are more likely to reflect biologically relevant changes (Figure 2F). In line with the density plots, the number of DMGs indicated that FC induces a greater number of hypermethylated CG-DMGs and hypomethylated CH-DMGs on day 7. We took the two most outstanding genes, *Mid1* and *H4c4*, from FC-induced CG-DMGs and CH-DMGs respectively as shown in Figure 2G. *Mid1* encodes the protein Midline-1, which belongs to the tripartite motif (TRIM) protein family that are post-translational modifiers. Midline-1 acts as a ubiquitin E3 ligase and can promote the polyubiquitination and proteasomal degradation of the catalytic subunit of PP2A, a memory regulator protein in the CNS.[51–53] We observed that on day 7, *Mid1* harbored a hypomethylated DMR located in intron 9 that is also a potential distal enhancer (from UCSC ENCODE cCREs track) specifically in FC mice. This hypomethylation returned to the baseline, similar to noFC control mice, on day 28 (Figure 2G). Another gene candidate from CH-DMGs is *H4c4*, which encodes a canonical histone H4 variant. The DMR identified for this gene is located in its regulatory regions (2745 bp upstream of the TSS), with hypermethylation specifically in FC animals compared to no FC animals, and this hypermethylation persisted from day 7 to day 28 (Figure 2G). We also noticed that this DMR associated with *H4c4* is closest (226bp away) to a FANTOM5 DPI peak (mm_113046.1), which represents a putative transcriptional start site (TSS). Notably, this TSS is active in the cortex of postnatal mice with MECP knockout (UCSC FANTOM5 database[54]), a model of Rett syndrome characterized by impaired cognitive functions. These examples suggest that

(C) (Top) density plots (area under the curve integrated to 1) and (bottom) black rug plots showing the density of CG- and CH-DMRs hypermethylation (0–1.0) or hypomethylation (−1.0 to 0). In the density plots, black lines are the distribution density of DMRs called from FC vs. no FC on day 7, and red lines are the distribution density of DMRs called from FC vs. no FC on day 28.

(D) Distribution of CG- (left) and CH-DMRs (right) in different genomic subregions for FC vs. no FC on day 7.

(E) Left, absolute count of CG- and CH-DMRs (differentially methylated regions) called from FC vs. no FC on day 7 and day 28. Right, absolute count of CG- and CH-DMGs (differentially methylated genes) called from FC vs. no FC on day 7 and day 28.

(F) Dot plots of DMGs from CG- and CH-DMRs. Each dot represents a DMR, plotted by methylation difference (x axis), with color indicating CG density. Arrows indicate the direction of methylation of FC (FC hypo, left; FC hyper, right). CG-DMRs in the top 3% by density and CH-DMRs in the top 2% by density were annotated with their corresponding genes.

(G) Representative CG- and CH-DMR examples show methylation differences between FC and no FC groups in the gene *Mid1* (intron 9 annotation based on transcript ENSMUST00000171433.7; this DMR of *Mid1* corresponds to DMR5 in Figure 5B) and *H4c4*. + indicates the forward strand, and – indicates the reverse strand. Methylation levels are displayed in heatmaps on a scale of 0–1.

(H) Significantly enriched biological processes of CG and CH-DMGs identified at day 7 in FC vs. no FC mice, performed using EnrichR. Dot size represents the number of genes overlapping with each GO term, and dot color represents the statistical significance (−log10 adjusted p-value). Overlap ratio is calculated as the number of hits divided by the total input DMGs.

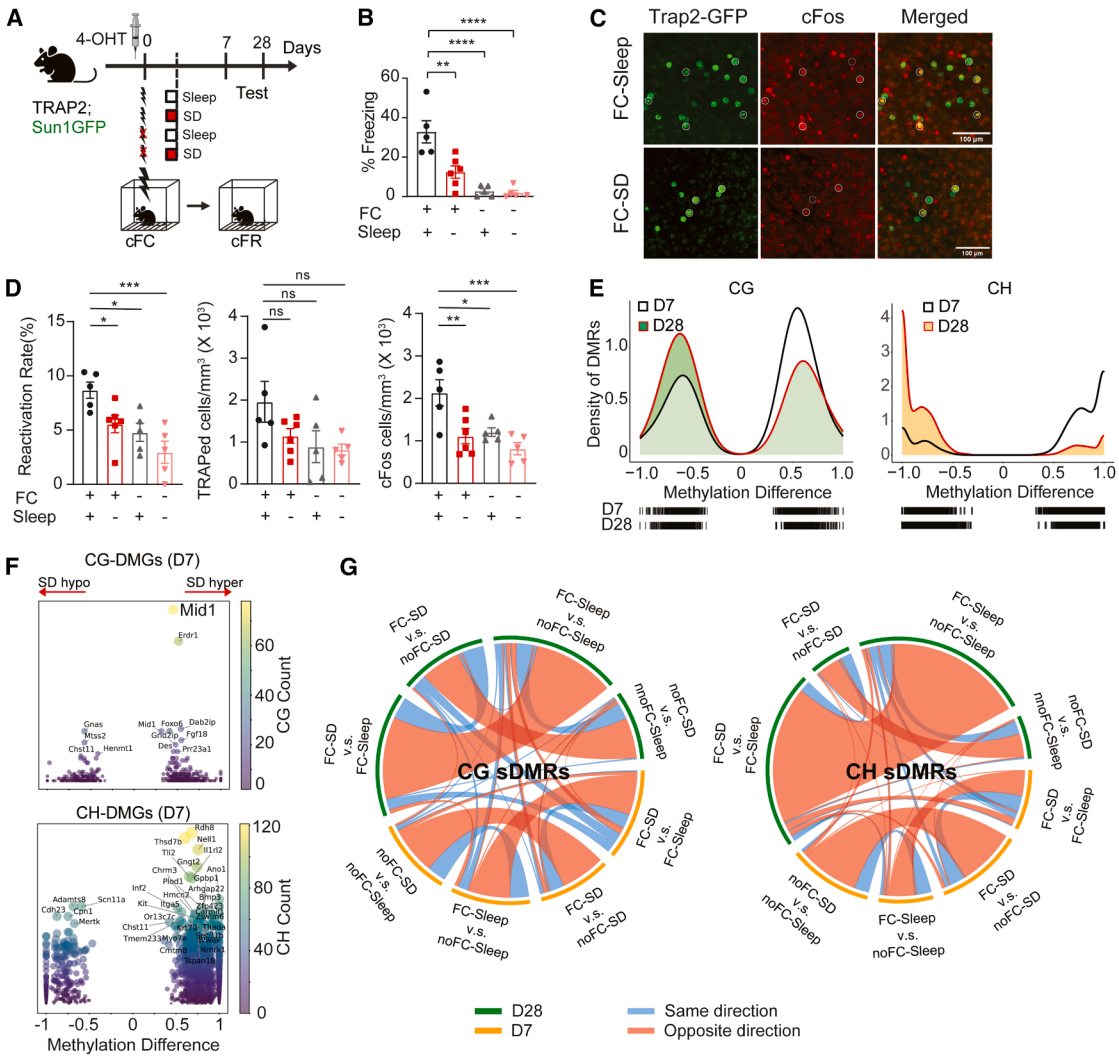


Figure 3. The impact of sleep deprivation on fear memory and DNA methylation

(A) Schematic of the experimental design. TRAP2; Sun1-GFP mice were injected with 4-hydroxytamoxifen (4-OHT) at the time of contextual fear conditioning (Day 0), followed by sleep or sleep deprivation (SD). 4-OHT was injected at 9:00 (ZT2), CFC or no-CFC (context exposure without shock) occurred at 14:00 (ZT7), and SD or no-SD (staying in the SD chamber with the treadmill off) followed immediately after CFC at 14:00 (ZT7). On day 7 or day 28, immediately after contextual fear recall, BLAs were extracted from these mice for WGBS, $n = 2$ per group.

(B) Averaged percentage of freezing behavior during cFR test on day 7 (one-way ANOVA followed by Post hoc Dunnett's multiple comparisons test of each group vs. FC-Sleep group: $F_{3,17} = 17.70$, $p < 0.0001$, $n = 5$–6 mice each group).

(C) Representative fluorescent images show TRAP2 labeled-GFP (green) and c-Fos protein (red) following sleep or SD in the BLA. Scale bars, 100 μm.

(D) Left, quantification of reactivation rate in BLA of four groups of mice (one-way ANOVA followed by Post hoc Dunnett's multiple comparisons test of each group vs. FC-Sleep group: $F_{3,17} = 7.435$, $p = 0.0022$). Middle, quantification of GFP+ cells in the BLA (one-way ANOVA followed by Post hoc Dunnett's multiple comparisons test of each group vs. FC-Sleep group: $F_{3,17} = 2.636$, $p = 0.0831$). Right, quantification of c-Fos+ cells in the BLA (one-way ANOVA followed by Post hoc Dunnett's multiple comparisons test of each group vs. FC-Sleep group: $F_{3,17} = 7.871$, $p = 0.0017$).

(E) (Top) density plots and (bottom) black rug plots showing the density of CG- and CH-DMRs. In the density plots, black lines are the distribution density of DMRs called from FC-Sleep vs. FC-SD on day 7, and red lines are the distribution density of DMRs called from FC-Sleep vs. FC-SD on day 28.

(F) Dot plots of DMGs from CG- and CH-DMRs. Each dot represents a DMR, plotted by methylation difference (x axis), with color indicating CG density. Arrows indicate the direction of methylation of FC-SD (FC-SD hypo, left; FC-SD hyper, right). CG-DMRs in the top 3% by density and CH-DMRs in the top 2% by density were annotated with their corresponding genes. Note that there are two dots representing different DMRs for Mid1, which correspond to DMR4 and DMR5 in Figure 5B.

(G) Chord diagram illustrates the shared differentially methylated regions (sDMRs) in the CG and CH contexts across all pairwise comparisons between experimental conditions at day 7 (D7) and day 28 (D28). Each segment on the circle corresponds to a group comparison. The arc length is proportional to the total shared DMRs (weighted) of that group with all other groups. Chords connecting segments represent overlapping DMRs, with thickness representing the Jaccard

(legend continued on next page)

learning-induced DMRs mark regulatory elements that are responsive to neuronal plasticity and memory formation.

Lastly, we examined the pathways associated with FC-induced DMGs to understand broadly the epigenetic responses following learning. Both CG- and CH-DMGs on day 7 are enriched in terms related to neuronal structure, connectivity, and signaling. CG-DMGs were enriched for terms including regulation of intracellular signal transduction, axonogenesis, synapse organization, and positive regulation of synaptic transmission, alongside cellular response to growth factor stimulus, suggesting that CG methylation differences are concentrated at genes regulating both axonal/synaptic function and neurotrophic signaling (Figure 2H). CH-DMGs were enriched for nervous system development, axonogenesis, axon guidance, cell-cell adhesion via plasma-membrane adhesion molecules, and extracellular matrix organization, indicating differential methylation in CH context at genes involved in structural neural organization and intercellular connectivity (Figure 2H). While GO terms such as nervous system development and axonogenesis may appear unexpected in the context of post-mitotic neurons, their enrichment among differentially CH-methylated genes more likely reflects the repurposing of developmental gene programs such as axonal remodeling and structural plasticity for mature neuronal functions.[55] Collectively, these results suggest that fear conditioning selectively recruits CG and CH methylation at gene sets governing distinct but complementary aspects of neuronal plasticity.

The impact of sleep deprivation on memory engrams and DNA methylation

To investigate how sleep affects the BLA engram, we applied total sleep deprivation (SD) after FC for 24 h in TRAP2;Sun1-GFP mice, allowing for putative engram cell labeling (GFP+) in the BLA and subsequent analysis (Figure 3A). Consistent with previous studies,[56,57] we observed that SD after learning impaired contextual fear memory, indicated by significantly less freezing behavior in SD mice during the recall test on day 7 (Figure 3B). Then, we examined the reactivation rate of labeled engram cells by co-localization of TRAP2-labeled GFP and c-Fos expression upon memory retrieval. We found that the BLA engram population was reduced in SD mice (Figure 3C), and this reduction was largely due to the reduced cFos+ populations during recall (Figure 3D), suggesting that sleep deprivation impaired the reactivation rate of fear memory engram cells in the BLA.

Next, we examined the consequences of sleep deprivation for learning-induced methylation remodeling. Compared to mice with normal sleep after FC, SD mice showed increases in DNA methylation (hypermethylation) at both CG and CH sites on day 7, and decreases in methylation (hypomethylation) on day 28 (Figure 3E). The numbers of CG- and CH-DMGs reflected this increase in hypermethylation in SD group (Figure 3F). Notably, the *Mid1* gene appeared at the top among these hypermethylated CG-DMGs in the SD group in Figure 3F, whereas it was the most hypomethylated gene after fear conditioning (Figure 2F), indicating the possibility that FC-induced DNA methylation changes were prevented or reversed by SD. To test this possibility broadly, we intersected all the DMRs identified from each comparison and defined the overlapping ones as shared DMRs (sDMRs). As shown in Figure 3G, the CG and CH sDMRs caused by sleep deprivation (FC-SD vs. FC-Sleep, at both day 7 and day 28) largely overlapped with those caused by fear conditioning (FC-Sleep vs. noFC-Sleep controls, at both timepoints), but the direction of methylation change was opposite, suggesting sleep deprivation disrupted the DNA methylation changes induced by fear learning. This inverse relationship became stronger from day 7 to day 28. We applied a reversal score to quantify this relationship and found that more than half of these sDMRs showed strong reversal by SD (Figure S5A; Table S3). These findings suggest that sleep deprivation partially reverses memory-related methylation changes, likely contributing to its detrimental effect on long-term memory.

We also characterized which learning-related functional pathways are impaired by SD via GO enrichment analysis of DMGs between FC-Sleep and FC-SD groups. Across both timepoints and methylation contexts (CG and CH), two distinct patterns emerged. CG-DMGs exhibited a broad and diverse range of enriched pathways, particularly on day 7, encompassing not only neuronal processes such as neuron development, axon guidance, synaptic organization, and regulation of neuronal synaptic plasticity, but also transcriptional regulation, cation transmembrane transport, and cytoskeletal organization (Figure S5B). This breadth likely reflects a widespread epigenetic response to SD at the early timepoint. By day 28, however, the CG-DMG enrichment profile narrowed considerably, converging on axonogenesis, axon guidance, and neuron projection guidance as the dominant terms (Figure S5C). This suggests that the initial broad CG methylation response progressively refines toward structural neuronal programs governing axonal connectivity and circuit organization. In contrast, CH-DMGs showed a remarkably consistent enrichment in intercellular signaling pathways including cell surface receptor signaling and cell-cell adhesion at both day 7 and 28 (Figures S5B and S5C), a pattern also evident in FC-induced CH-DMGs (Figure 2H). By day 28, this enrichment further extended toward synapse assembly, glutamatergic synaptic transmission, and modulation of chemical synaptic transmission (Figure S5C). This consistency across both fear learning and sleep deprivation contexts suggests that CH methylation changes selectively target intercellular signaling programs, potentially reflecting a core epigenetic mechanism underlying experience-dependent neural communication. Together, these data demonstrate that sleep deprivation disrupts distinct CG and CH methylation programs in BLA putative engram cells.

To ensure these methylation events are specific to fear engram cells, we performed WGBS using GFP- cells. Principal component analysis (PCA) of CG and CH methylation showed that

Index and color indicating directionality. Red chords represent sDMRs changing in opposite directions (e.g., hypermethylated in one comparison and hypomethylated in the other), while blue chords represent sDMRs changing in the same direction. Statistical significance of each overlap was assessed by an empirical permutation test (see methods for a detailed description and Table S2 for *p*-values). Data are shown as mean ± SEM. $^{*}p < 0.05$, $^{**}p < 0.01$, $^{***}p < 0.001$, and $^{****}p < 0.0001$; ns, not significant.

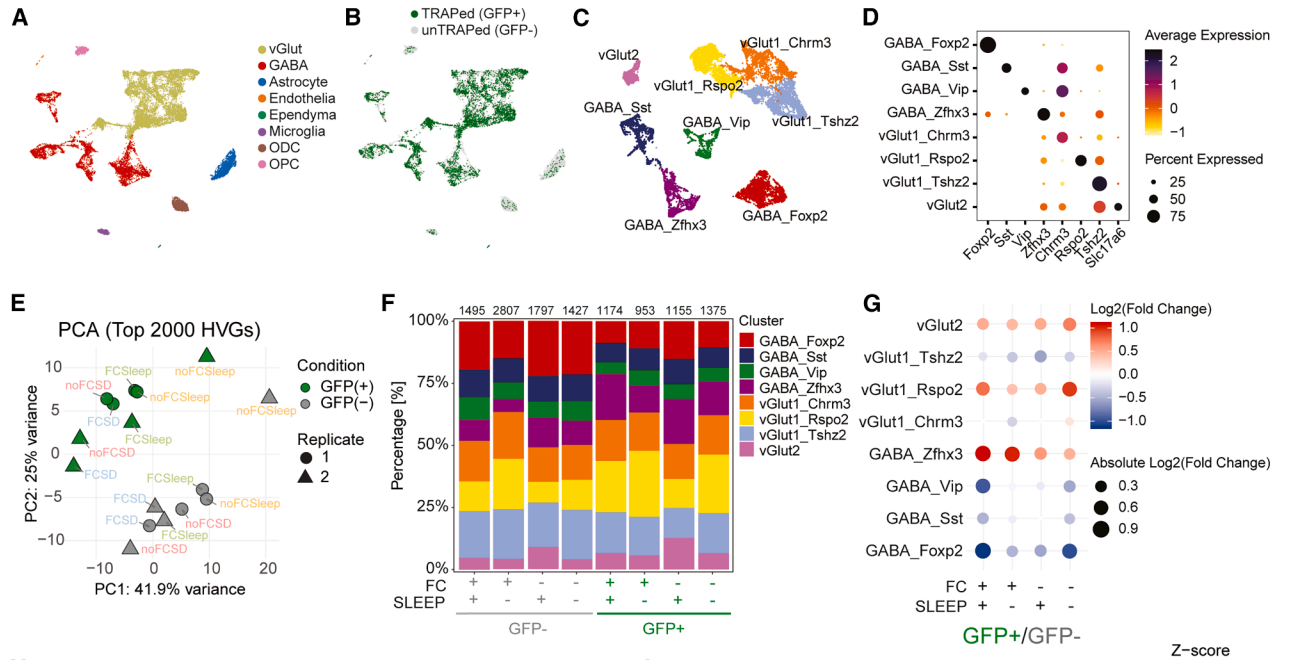


Figure 4. Transcriptomic profiling of BLA engram neurons

(A) UMAP clustering of all BLA cells sorted from both GFP+ and GFP-. Each dot represents a single nucleus, colored by cell type. Nuclei were pooled from 4 mice per group across 4 experimental groups with the same schematics as WGBS (FC-Sleep/FC-SD/noFC-Sleep/noFC-SD; BLAs were extracted from these mice 1hr after contextual fear recall on day 7), with 2 independent replicates (total $n = 32$ mice). A total of 12,183 nuclei were clustered into 8 major cell types: excitatory neurons (vGlut), inhibitory neurons (GABA), astrocytes, endothelial cells, ependymal cells, microglia, oligodendrocytes (ODC), and oligodendrocyte precursor cells (OPC).

(B) Distribution of GFP+ cells (green) and GFP- (gray) cells in the UMAP.

(C) UMAP clustering of BLA neuronal subtypes from GFP+ and GFP-.

(D) Dot plot shows the expression of selected marker genes across cell clusters. Color represents average expression, and dot size represents the neuronal percentage of the marker genes.

(E) Principal component analysis (PCA) was performed on the expression profiles of 2000 highly variable genes (HVGs) across different experimental groups and across 2 independent replicates. Green dots label GFP+ groups and gray dots label GFP- groups.

(legend continued on next page)

GFP− cells form a tight, invariant cluster regardless of condition or timepoint, confirming that epigenomic divergence is selective to GFP+ neurons (Figure S3D). Consistent with this, the vast majority of DMRs identified in GFP+ cells showed minimal overlap with those in GFP− cells, and the learning-induced DMGs were different between GFP+ and GFP- cells (Figures S6A and S6B). Notably, the PCA plots for CG and CH methylation also revealed that the methylome of GFP+ neurons from FC-SD and no FC control groups clustered together on day 28, not day 7, while FC-Sleep group clearly separated from all these groups (Figure S3D). This observation supports a persistent, consolidation-related methylation signature on day 28.

Transcriptomic profiling of BLA putative engram neurons

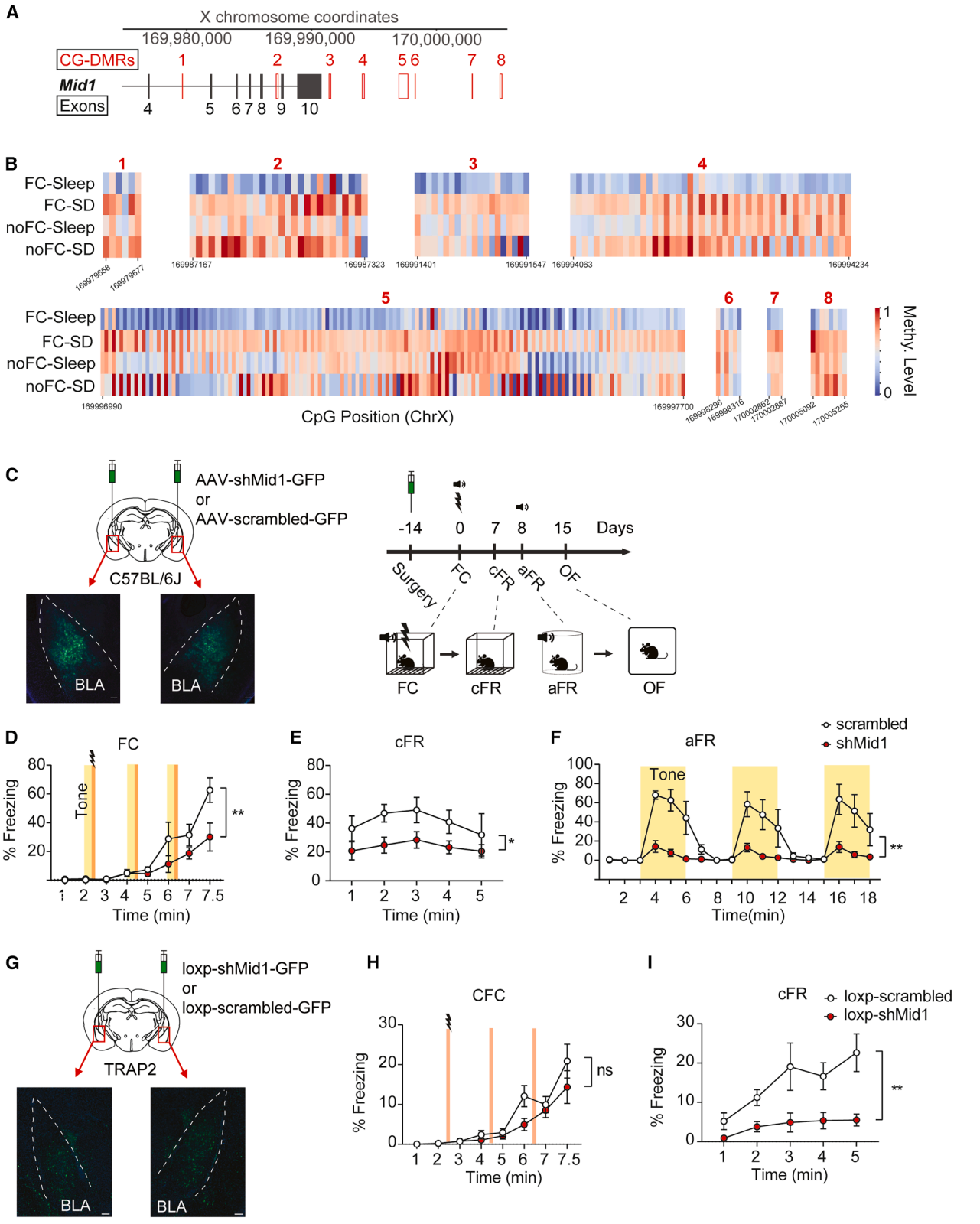
To explore the functional consequence of DNA methylation, we examined the transcriptome of BLA putative engram cells using PIP-seq, a well-established single-cell RNA sequencing protocol optimized for low-input samples.[58] Using TRAP2;Sun1-GFP mice in the same experimental paradigm as WGBS, we isolated both GFP+ (putative engram) and GFP− (control) nuclei by FANS (Figure S7A) from BLA across four groups (FC-Sleep, FC-SD, no FC-Sleep, and no FC-SD) 1-h post-recall to capture transcriptional responses. Two independent replicates were performed with 4 mice pooled per group, yielding a total of 12,183 nuclei. Nuclei from both replicates showed consistent cluster distributions (Figure S7B). As shown in Figure 4A, these cells covered all major cell types of BLA including glutamatergic neurons (vGlut), GABAergic neurons (GABA), astrocytes, endothelial cells, ependymal cells, microglia, oligodendrocytes (ODC), and oligodendrocytes progenitor cells (OPC). While GFP- cells span across all cell types, GFP+ are mainly composed of neurons (Figures 4B and S7C). Thus, our following analysis mainly focused on neurons. All these neurons were clustered into eight subtypes with four glutamatergic and four GABAergic (Figures 4C and 4D) using both conventional and most-expressed gene markers shown in Figure S7D. In brief, the four glutamatergic clusters labeled with top-expressed genes are: vGlut1_Rspo2, vGlut1_Chrm3, vGlut1_Tshz2, and vGlut2. The vGlut1_Rspo2 cluster contains genes *Rspo2* and *Sema3e* that are reported previously for encoding aversive stimuli.[21–23] *Lmo3* and *Etv1*, also reported previously as potential BLA markers, are expressed in both the vGlut1_Rspo2 and vGlut1_Chrm3 clusters. *Mef2c*, *Lypd1*, and *Satb1*, which are also potential BLA markers, were reported to be expressed in the vGlut1_Tshz2 cluster, a distinct one from the vGlut1_Rspo2 and vGlut1_Chrm3 clusters.[59,60] For GABAergic clusters, there are: GABA_Foxp2, GABA_Sst, GABA_Vip, and GABA_Zfhx3. *Cck*, encoding for cholecystokinin that modulates anxiety,[61] was marked in the GABA_Vip gene expression profile in our dataset. Interestingly, PCA clustering of top 2000 highly variable genes (HVGs) showed that GFP+ and GFP- populations can be well separated, which indicates that GFP+ and GFP- neuronal populations are transcriptionally distinct (Figure 4E). This is consistent with previous studies showing that engram cells contain intrinsic properties that set them apart from non-engram cells.[62–65] All the four behavioral groups showed comparable cell-type composition within both GFP+ and GFP- neuronal population (Figures 4F and 4G), suggesting no engram-specific neuronal cell type.

Given the limited cell numbers within individual clusters, we focused our differential gene expression analysis on two major cell types, vGlut and GABA neurons, to maximize statistical power. As shown in Figures 4H and 4I, DEGs identified between the four experimental groups within either vGlut or GABA neurons were clustered based on their dynamic expression pattern across conditions, generating six distinct DEG clusters in each cell type. In FC-Sleep GFP+ (putative engram) cells, several functional categories, particularly synapse organization and RNA splicing, were enriched across multiple clusters spanning different expression dynamics. This indicates that genes within these broad processes are not uniformly regulated. Instead, they are segregated into subsets with divergent trajectories. Synapse organization genes were represented among the most strongly upregulated clusters (vGlut.C1, C2; GABA.C1, C4), as well as among clusters showing moderate changes (vGlut.C4) and mild downregulation (vGlut.C6; GABA.C6). RNA splicing genes similarly spanned the moderately changed (vGlut.C3; GABA.C2) and mildly downregulated (vGlut.C5) clusters. Notably, for both excitatory and inhibitory neurons, the C1 clusters showed the most selective upregulation in FC-Sleep GFP+ cells. Upon SD, their increased expression was interfered with and returned to or below noFC-Sleep GFP+ control levels. In GABA neurons, the moderately changed and mildly downregulated clusters additionally included genes related to neuronal morphogenesis and cellular homeostasis in C5 (e.g., dendrite development, small GTPase-mediated signal transduction, calcium ion homeostasis), alongside genes involved in mitochondrial energy metabolism in C3 (e.g., oxidative phosphorylation, mitochondrial ATP synthesis, electron transport chain). Together, these results suggest that the clustering captures finer-grained co-expression substructure within broader pathways, and that the synapse-related genes most strongly induced by FC-Sleep in engram cells are also the most dependent on sleep for their maintenance. In addition to GFP+ cells, GFP- cells also showed substantial, but distinct, transcriptomic changes among four behavior groups (Figures 4H and 4I). For all the clusters (except GABA.C1&C6) within GFP- populations, noFC-Sleep and noFC-SD exhibited contrasting differences, whereas FC-Sleep and FC-SD converged in this regard, suggesting that

(F) Stacked bar graphs show the relative proportions of neuronal subtypes across samples in different experimental groups. Each column represents one group, with the total number of nuclei indicated above.

(G) Dot plot shows proportions of neuronal subtypes involved in GFP+ compared to GFP- across experimental groups. Dot color indicates the direction and magnitude of the log2 fold change. Dot size reflects the absolute log2 fold change, with larger dots indicating greater divergence between GFP+ and GFP− populations.

(H and I) Heatmaps show normalized gene expression (*Z* score) of differentially expressed genes (DEGs) in glutamatergic (H) and GABAergic BLA neurons (I) with expression patterns (red lines in the left sub-panels) and annotated GO terms across experimental groups.



(legend on next page)

fear conditioning shifts GFP- neurons away from sleep-dependent biological responses. These distinct patterns in GFP- cells imply that fear memory reconfigures the transcriptional landscape of a broader neuronal population beyond engram cells in BLA.

Collectively, these PIP-seq results reveal that sleep and fear conditioning interact to shape distinct transcriptional programs across the BLA cells. Within putative engram cells, sleep supports memory consolidation by upregulating synaptic and dendritic regulatory programs. These programs are disrupted by SD, returning to noFC control levels. RNA processing, regulation of protein stability, and oxidative metabolism programs are instead elevated by SD, accompanied by memory disruption.

Methylation target *Mid1* in the BLA is required for fear learning and memory

To explore how DNA methylation contributes to fear memory in the BLA, we integrated the DNA methylome and single-cell transcriptome to identify genes that harbor both changes in DNA methylation and transcription, likely contributing to fear memory. As shown in Figure S8A, Intersecting Day-7 DMGs from WGBS with DEGs from PIP-seq, GFP+ cells showed the highest DEG-DMG overlap in the FC-Sleep vs. FC-SD and FC-Sleep vs. noFC-Sleep comparisons, particularly among vGlut DEGs, while SD-only comparisons (FC-SD vs. noFC-SD; noFC-SD vs. noFC-Sleep) yielded little to no overlap. GFP− cells showed no such trend, confirming these molecular changes are engram-specific. Among the intersected genes, *Mid1* possessed the strongest differentially methylated loci (Figures 2F and 3F) associated with dynamic gene expression changes in the putative BLA engrams (Figure S8B). The *Mid1* locus (RefSeq NM_010797) includes 10 exons spanning ∼300 kb on the positive strand of chromosome X (Figure 5A), and harbors eight identified CG-DMRs spanning its gene body and near its 3′ locus, all showing FC-Sleep-specific hypomethylations that are disrupted by SD (Figure 5B). To further examine the transcriptional response of *Mid1* to learning, we performed bulk RNA-seq and found *Mid1* expression in the BLA decreased within 1–4 h after learning (Figure S8C). These observations led us to focus on *Mid1* as a DNA methylation target in the BLA.

To dissect the functional significance of *Mid1* in learning and memory, we performed three *Mid1* knockdown experiments in the BLA with shRNA validated via RT-qPCR (Figure S9A) and RNAscope (Figure S9B). First, bulk BLA *Mid1* knockdown prior to fear conditioning impaired both learning and subsequent memory retrieval as shown in Figures 5C–5F, with no effect on general locomotion or anxiety in the open field test (Figures S9G–S9N). To dissociate learning from memory consolidation, we next performed bulk BLA *Mid1* knockdown with submaximal viral expression, such that learning remained intact while memory retrieval was still impaired (Figures S9C–S9F). Finally, to determine whether *Mid1* function within putative engram neurons is required for fear memory, we selectively knocked down *Mid1* in fear conditioning-activated cells using a loxP-shRNA construct in TRAP2 mice. We demonstrated that engram-specific knockdown of *Mid1* in the BLA was sufficient to impair memory retrieval, as shown in Figures 5G–5I. Together, these results implicate an essential role of *Mid1*, a gene previously uncharacterized in engram biology, in fear memory within BLA putative engram populations.

We noticed the hypomethylation of *Mid1* in FC-Sleep was associated with the downregulation of *Mid1* expression, which is distinct from the conventional model where hypermethylation is associated with gene silencing. So we examined the relationship between *Mid1* methylation and transcription using GSK3685032,[66] a DNA methylation inhibitor, *in vitro*. GSK3685032 treatment resulted in reduced methylation at the *Mid1* locus, specifically at the DMRs identified from our WGBS analysis, and a decrease in *Mid1* RNA expression (Figure S10). These results suggest that, at these DMRs, methylation of *Mid1* may play an activating rather than a repressive role in transcriptional regulation.

DISCUSSION

The molecular mechanism by which post-learning sleep consolidates fear memory at the level of individual memory-encoding neurons is unknown. While DNA methylation is established as a critical regulator of hippocampal and cortical memory consolidation,[34,36,45,46] epigenetic investigations of BLA, a structure essential for the acquisition and long-term storage

Figure 5. *Mid1* in BLA is required for learning and memory

(A) Genomic location of CG-DMRs identified from *Mid1* gene locus (NM_010797/ENSMUST00000112104.7).

(B) Heatmaps of methylation levels of eight CG-DMRs from the *Mid1* gene across four experimental groups of day 7. DMR4 and DMR5 are also found in the dot plot in Figure 3F, and DMR5 is also represented in Figure 2G.

(C) Left, schematic of AAV injection (green) and expression of shRNA targeting the *Mid1* gene in bilateral BLA. Scale bars, 100 μm. Right, schematic of experimental design. Mice received AAV injections at day −14, followed by auditory fear conditioning (aFC) on day 0, contextual fear recall (cFR) on day 7, auditory fear recall (aFR) on day 8, and open field testing (OF) on day 15.

(D) Freezing behavior during aFC. Shaded bars indicate 30s tones (yellow) and 2s footshocks (orange) (two-way RM ANOVA: treatment × time interaction: $F_{7,70}$ = 3.87, p = 0.0013; n = 5 for control group and n = 7 for knockdown group).

(E) Freezing behavior during cFR test on day 7 (two-way RM ANOVA: treatment, $F_{1,10}$ = 5.48, p = 0.041).

(F) Freezing behavior during aFR test on day 8 (two-way RM ANOVA: treatment, $F_{1,10}$ = 14.13, p = 0.0037).

(G) Schematic of AAV injection and expression of Cre-dependent shRNA targeting *Mid1* gene in bilateral BLA (green) to knock down *Mid1* in cells activated during contextual fear conditioning (cFC) via TRAP2 mice. Scale bars, 100 μm.

(H) Freezing behavior during FC. Shaded bars indicate footshocks (orange) (two-way RM ANOVA: treatment, $F_{1,18}$ = 2.226, p = 0.153; n = 9 for control group injected with AAV-loxp-scrRNA-GFP and n = 11 for knockdown group injected with AAV-loxp-shMid1-GFP). 4-OHT was injected immediately after FC.

(I) Freezing behavior during cFR test on day 7. The asterisk indicates the main effect of treatment was observed (two-way RM ANOVA: treatment, $F_{1,15}$ = 9.9, p = 0.0067; n = 9 for control group and n = 8 for knockdown group). Data are shown as mean ± SEM. *p < 0.05, **p < 0.01, ***p < 0.001, and ****p < 0.0001; ns, not significant.

of fear memories, have been absent. Here, we establish that sleep-dependent DNA methylation remodeling within BLA fear engram cells is functionally required for fear memory consolidation, demonstrating that post-learning sleep loss impairs memory at both the cellular and molecular levels. Using engram-specific and BLA-regional DNMT manipulations, we demonstrate that DNMTs are required within the BLA, with supporting evidence from engram-specific *Dnmt3a* deletion consistent with this requirement in memory. We profile the BLA engram methylome and transcriptome at single-cell resolution across learning and sleep conditions at day 7 and day 28, revealing that learning induces coordinated and temporally dynamic CpG and neuron-specific CpH methylation changes in engram cells. Interestingly, genes with CpG changes enrich for intracellular pathways, while CpH-affected genes enrich for intercellular pathways. PCA of both contexts of methylomes shows that engram cells undergo larger changes than non-engram cells, and that post-learning sleep establishes a new methylome landscape by day 28 that other groups, including sleep-deprived animals, fail to establish. This indicates that adult CpH methylation is neither a byproduct of elevated DNMT activity nor a static, developmentally accumulated fixed mark,[48,49,67] but is functionally engaged during learning and memory together with CpG methylation. Furthermore, we found that learning-induced methylation changes are selectively impaired by post-learning sleep deprivation, suggesting that sleep gates epigenetic programs operating within defined memory-encoding neurons. Integration of engram-specific methylome and transcriptome data reveals *Mid1*, a gene whose methylation and expression are regulated by learning and sleep. We found engram-specific knockdown of *Mid1* in the BLA is sufficient to impair fear memory consolidation. Together, these findings reveal sleep-dependent methylation remodeling as a candidate mechanism in BLA-dependent fear memory consolidation.

BLA-regional and engram-specific DNMT requirements for fear memory

DNMTs have been previously implicated in hippocampus-dependent memory consolidation, including spatial and contextual fear memory.[34,36,45,68,69] Our work establishes that DNMTs in the BLA are required for fear memory. Viral knockdown of both *Dnmt3a* and *Dnmt1* in the BLA impaired contextual and auditory fear memory more effectively than engram-specific *Dnmt3a* deletion alone, suggesting that both methyltransferases contribute to BLA-dependent fear memory function.[43] Temporal control was critical for dissociating the roles of DNMTs in learning versus consolidation. When shRNAs were delivered prior to learning, behavioral impairments were observed at both acquisition and recall, consistent with the role of DNMTs in long-term potentiation (LTP) and synaptic regulation.[39,41,42] When mice were fear-conditioned shortly after viral injection, learning performance was normal, yet recall remained impaired. This demonstrates that BLA DNMTs are required for memory consolidation or storage independently of their role in initial learning. Together, these manipulations establish that DNMT activity within the BLA is required at multiple stages of fear memory processing, and that *Dnmt3a* and *Dnmt1* act in concert to support this function. Consistent with a role of DNA methylation in stable, consolidation-related epigenetic remodeling, the temporal dynamics of engram methylation further support a persistent, learning-associated signature rather than a transient consequence of sleep manipulation: at Day 28, the methylomes of FC-SD converged with no FC groups, while FC-Sleep remained distinct, revealing a pattern arguing against a delayed effect by sleep loss, which would instead predict SD groups remaining separable from non-SD groups at this later timepoint. This convergence was absent on Day 7, indicating that the Day 28 landscape reflects durable, consolidation-related methylation changes. Moreover, the DNMT-dependent mechanism we describe in the BLA fear engram is unlikely to be restricted to fear memory. Beyond contextual fear conditioning, DNMT activity has been shown to be required for spatial memory in the hippocampus,[43] object recognition memory,[68] and reward-associated memory.[70] Our findings reveal that BLA engram methylation is dynamically shaped by sleep, identifying post-learning sleep as a physiological gate for DNMT-dependent epigenetic consolidation. It is possible that DNMT-dependent epigenetic programming is a broadly conserved feature of long-term memory consolidation across brain regions and memory systems during sleep, while the specific molecular targets engaged and the physiological signals that gate this programming may differ across circuits. Future work in this direction is needed to test this.

Integration of methylation and transcriptome data at engram resolution

The pairing of engram-specific WGBS with engram-specific single-nucleus transcriptomics enables direct integration of epigenetic and transcriptional data within the same labeled cell population across behavioral conditions. This allows us to construct a multi-omic molecular atlas of the BLA fear engram and to identify affected genes, such as *Mid1*. For single-nucleus transcriptomics, we initially hypothesized that FC-Sleep engrams would exhibit learning-specific transcriptomic profiles distinct from those of other groups at a cell-type-specific level. However, limited cell numbers reduced our statistical power, preventing robust cell type-specific differential expression analysis. Nevertheless, vGlut.C1 and GABA.C1 clusters showed relatively higher expression of some synapse-related genes in FC-Sleep GFP+ neurons compared to other GFP+ groups and GFP- neurons, though other GFP+ groups also showed moderate increases. Therefore, memory-related transcriptional responses are unlikely to be driven by a single critical gene or cell type. Rather, engram transcription likely reflects the combined gene expression patterns across multiple genes and neuronal populations.

Methylation-regulated effectors of fear memory consolidation: *Mid1* and beyond

By overlapping learning- and sleep-dependent DMGs and DEGs within BLA engram cells, we identified *Mid1* as a candidate gene whose DNA methylation and transcriptional regulation converge across both molecular layers. Notably,

learning-induced demethylation of *Mid1* was disrupted by sleep deprivation, linking its epigenetic state to the sleep-dependent consolidation window. Loss-of-function mutations in *Mid1* during development cause X-linked Opitz G/BBB syndrome, a disorder marked by midline structural defects and intellectual disability in approximately 30–50% of affected males.[71,72] Additionally, MID1 protein regulates synaptic plasticity during hippocampal development.[72] Given that learning induces a reduction in *Mid1* expression, whereas a more severe loss-of-function at both bulk and engram-specific levels in the BLA also impairs learning and memory, the precise molecular mechanism by which *Mid1* contributes to fear memory formation appears more complex than a simple dose-dependent relationship and remains an open question for future investigation. Based on the current knowledge, we speculate three potential, though not mutually exclusive pathways: (1) MID1 mediates ubiquitin-dependent degradation of PP2A subunits, thereby regulating the phosphorylation of synapse-related proteins such as tau[51,53,73]; (2) since MID1 is required for axonal projection during development,[74] it could contribute to axonal restructuring upon learning in adults; (3) the MID1-PP2A interaction also regulates mTOR1 signaling,[75] a central hub of neuronal plasticity. Our study of *Mid1* provides a framework for systematic investigation of methylation target genes in memory engrams. While *Mid1* emerged as our top candidate, other memory-related genes with reported learning-dependent methylation changes in the hippocampus, such as *Ppp1cc* and *Reln*,[36] showed distinct patterns in the BLA: *Reln* remained a DMG, with multiple differentially methylated CpG and CpH sites of modest sizes in intronic regions, whereas *Ppp1cc* did not meet our DMG criteria. This divergence underscores a central theme of our study: that the engram methylome follows region-specific rather than a universal logic, reinforcing the value of BLA-specific profiling for identifying functionally relevant targets such as *Mid1*.

Beyond *Mid1*, our integrated dataset also reveals a broader list of candidate genes whose methylation and expression are dynamically regulated by learning and/or sleep in BLA engram cells. Follow-up studies of these candidates will further substantiate the contribution of DNA methylation to memory function and help dissect which changes reflect direct methylation-driven transcriptional regulation versus other epigenetic mechanisms acting in parallel. More broadly, our behavioral focus on fear memory provides a well-characterized and translatable model but leaves open questions on whether the BLA engram methylation program described here governs other emotional memories, and whether the specific fear-engram methylome signature is conserved across amygdala subregions or generalizes to other medial temporal lobe structures. The BLA is a canonical substrate for threat memory and is dysregulated in PTSD and anxiety disorders, both highly associated with sleep disturbances. Identifying sleep-dependent epigenetic mechanisms within BLA fear engrams may therefore have relevance for understanding how sleep disruption in trauma-exposed individuals contributes to the pathological persistence of fear memories.

Limitations of the study

(1) This study uses a 24-h total sleep deprivation to probe the role of sleep in BLA-dependent fear memory consolidation as the consolidation window is not well-defined for BLA, yet prolonged SD remains an inherently non-specific stress paradigm whose effects cannot be fully dissociated from sleep loss itself; (2) while the fear recall test was needed to behaviorally validate successful memory consolidation, it may introduce retrieval- and fear-related transcriptional response on top of the more persistent post-learning epigenetic and transcriptional state that the current design is unable to take apart; (3) current data has not established a direct link between *Mid1*-locus specific methylation and learning/memory, so an *in vivo* locus-specific methylation editing of *Mid1* together with learning/memory examination is a priority for our future work.

RESOURCE AVAILABILITY

Lead contact

Requests for further information and resources should be directed to and will be fulfilled by the lead contact Shawn Liu (sl4738@cumc.columbia.edu).

Materials availability

No unique materials were generated in this study.

Data and code availability

Raw sequencing data for bulk RNA-seq, PIP-seq, and WGBS have been deposited at the NCBI Sequence Read Archive under BioProject SRA: PRJNA1304968. Processed data have been deposited at GEO under accession numbers GEO: GSE348488, GSE348480, GSE348542, and GSE348705. All data are publicly available as of the date of publication. Accession numbers are also listed in the key resources table. This paper does not report original code. All additional information required to reanalyze the data reported in this paper is available from the lead contact upon reasonable request.

ACKNOWLEDGMENTS

We thank Dr. Guoping Fan at UCLA and Dr. Jian Feng at Florida State University for sharing the *Dnmt3a*$^{fl/fl}$ mice. This work was supported by Columbia University Startup Packages and grants from NIH (R01NS126185, R01MH134519, R01MH142809, and R01NS129997), Columbia RISE award, and Chan Zuckerberg Initiative. We thank Michael Kissner at the Columbia Stem Cell Initiative Flow Cytometry Core for technical support in cell sorting. We thank Humberto Avila and Dr. Luke Hammond from Zuckerman Institute's Cellular Imaging Platform for instrument use, technical advice, and analysis. We thank Bryan Uceda-Alvarez, Leslie Yao, Kitti Rusznák, Katherine Lee, and Andre Adonnino for their assistance with the initial exploratory phases, and Dr. Wanqi Wang, Sarah Chung, Sophia Tong and Scarlett Dellacona for their support during the late-stage exploratory phases of this project. We thank Roger Cole for their assistance in optimizing the DNMT3A immunostaining protocol. We thank Veria Puerta-Alvarado and Mira Nayak for their support in grant-linked pilot testing and reviewer response data, respectively. We thank Dr. Rene Hen, Dr. Christine Denny, Dr. Darcy Peterka, and members of the Peng and Liu laboratories for helpful discussions.

AUTHOR CONTRIBUTIONS

X.C., Y.P., and X.S.L. conceived the project. X.C. performed the majority of experiments and data analysis. F.R. performed data analysis on PIP-seq. A.M. assisted with genotyping, WGBS sample collections, imaging, and analysis for cFos experiments and DNMT3A immunostaining experiments. R.P. performed *in vitro* experiments and analysis related to *Mid1*. R.W. performed RNAscope experiments and analysis. L.Z. assisted with immunostaining and histology of engram *Mid1* KD experiments and TRAP2;*Dnmt3a*$^{fl/fl}$ validation.

M.J. assisted with behavioral analysis. K.Y. assisted with PIP-seq experiments. X.C., W.Z., H.L., Y.P., and X.S.L. wrote the paper.

DECLARATION OF INTERESTS

X.S.L. is a co-founder of Epitor Therapeutics. Other authors declare that they have no competing interests.

STAR★METHODS

Detailed methods are provided in the online version of this paper and include the following:

- KEY RESOURCES TABLE
- EXPERIMENTAL MODEL AND STUDY PARTICIPANT DETAILS
  - Animals
  - Cell lines
- METHOD DETAILS
  - Viral injection
  - Animal behavior
  - TRAP2;Sun1-GFP mice behavioral timeline
  - Histology, immunohistochemistry, and cell counting
  - Tissue preparation for WGBS and PIP-seq
  - Nuclei isolation
  - Fluorescence-activated nuclear sorting (FANS)
  - Whole-genome bisulfite sequencing (WGBS)
  - DMR genomic regions annotations and enrichment
  - DMGs pathway enrichment analysis
  - DMRs overlap with pairwise comparisons
  - DNA methylation reversal score within shared DMRs (sDMRs)
  - PIPseq for single nuclei RNA sequencing
  - Processing PIP-seq data and initial quality control
  - Dimensionality reduction, clustering, and additional filtering
  - Differential gene expression analysis
  - Single cell proportion test
  - Bulk RNA sequencing
  - qRT-PCR
  - RNAscope for validating *Mid1* knockdown
  - GSK3685032 treatment
- QUANTIFICATION AND STATISTICAL ANALYSIS

SUPPLEMENTAL INFORMATION

Supplementary data related to this article can be found online at https://doi.org/10.1016/j.celrep.2026.118190.

Received: September 24, 2025
Revised: August 6, 2026
Accepted: October 5, 2026

REFERENCES

1. Kandel, E.R., Dudai, Y., and Mayford, M.R. (2014). The molecular and systems biology of memory. Cell *157*, 163–186. https://doi.org/10.1016/j.cell.2014.03.001.
2. Abel, T., Havekes, R., Saletin, J.M., and Walker, M.P. (2013). Sleep, plasticity and memory from molecules to whole-brain networks. Curr. Biol. *23*, R774–R788. https://doi.org/10.1016/j.cub.2013.07.025.
3. Rasch, B., and Born, J. (2013). About Sleep's Role in Memory. Physiol. Rev. *93*, 681–766. https://doi.org/10.1152/physrev.00032.2012.
4. Born, J., Rasch, B., and Gais, S. (2006). Sleep to remember. Neuroscientist *12*, 410–424. https://doi.org/10.1177/1073858406292647.
5. Diekelmann, S., and Born, J. (2010). The memory function of sleep. Nat. Rev. Neurosci. *11*, 114–126. https://doi.org/10.1038/nrn2762.
6. Denny, C.A., Lebois, E., and Ramirez, S. (2017). From Engrams to Pathologies of the Brain. Front. Neural Circuits *11*, 23. https://doi.org/10.3389/fncir.2017.00023.
7. Roy, D.S. (2022). Brain-wide mapping reveals that engrams for a single memory are distributed across multiple brain regions. Nat. Commun. *13*, 1799.
8. Liu, X., Ramirez, S., Redondo, R.L., and Tonegawa, S. (2014). Identification and Manipulation of Memory Engram Cells. Cold Spring Harb. Symp. Quant. Biol. *79*, 59–65. https://doi.org/10.1101/sqb.2014.79.024901.
9. Poo, M.M., Pignatelli, M., Ryan, T.J., Tonegawa, S., Bonhoeffer, T., Martin, K.C., Rudenko, A., Tsai, L.H., Tsien, R.W., Fishell, G., et al. (2016). What is memory? The present state of the engram. BMC Biol. *14*, 40. https://doi.org/10.1186/s12915-016-0261-6.
10. Tonegawa, S., Liu, X., Ramirez, S., and Redondo, R. (2015). Memory Engram Cells Have Come of Age. Neuron *87*, 918–931. https://doi.org/10.1016/j.neuron.2015.08.002.
11. Liu, X., Ramirez, S., Pang, P.T., Puryear, C.B., Govindarajan, A., Deisseroth, K., and Tonegawa, S. (2012). Optogenetic stimulation of a hippocampal engram activates fear memory recall. Nature *484*, 381–385. https://doi.org/10.1038/nature11028.
12. Kitamura, T., Ogawa, S.K., Roy, D.S., Okuyama, T., Morrissey, M.D., Smith, L.M., Redondo, R.L., and Tonegawa, S. (2017). Engrams and Circuits Crucial for Systems Consolidation of a Memory. Science *356*, 73–78. https://doi.org/10.1126/science.aam6808.
13. DeNardo, L.A., Liu, C.D., Allen, W.E., Adams, E.L., Friedmann, D., Fu, L., Guenthner, C.J., Tessier-Lavigne, M., and Luo, L. (2019). Temporal evolution of cortical ensembles promoting remote memory retrieval. Nat. Neurosci. *22*, 460–469. https://doi.org/10.1038/s41593-018-0318-7.
14. Denny, C.A., Kheirbek, M.A., Alba, E.L., Tanaka, K.F., Brachman, R.A., Laughman, K.B., Tomm, N.K., Turi, G.F., Losonczy, A., and Hen, R. (2014). Hippocampal memory traces are differentially modulated by experience, time, and adult neurogenesis. Neuron *83*, 189–201. https://doi.org/10.1016/j.neuron.2014.05.018.
15. Han, J.H., Kushner, S.A., Yiu, A.P., Hsiang, H.L.L., Buch, T., Waisman, A., Bontempi, B., Neve, R.L., Frankland, P.W., and Josselyn, S.A. (2009). Selective erasure of a fear memory. Science *323*, 1492–1496. https://doi.org/10.1126/science.1164139.
16. Rashid, A.J., Yan, C., Mercaldo, V., Hsiang, H.L.L., Park, S., Cole, C.J., De Cristofaro, A., Yu, J., Ramakrishnan, C., Lee, S.Y., et al. (2016). Competition between engrams influences fear memory formation and recall. Science *353*, 383–387. https://doi.org/10.1126/science.aaf0594.
17. Zhou, Y., Won, J., Karlsson, M.G., Zhou, M., Rogerson, T., Balaji, J., Neve, R., Poirazi, P., and Silva, A.J. (2009). CREB regulates excitability and the allocation of memory to subsets of neurons in the amygdala. Nat. Neurosci. *12*, 1438–1443. https://doi.org/10.1038/nn.2405.
18. Davis, M. (1992). The role of the amygdala in fear and anxiety. Annu. Rev. Neurosci. *15*, 353–375. https://doi.org/10.1146/annurev.ne.15.030192.002033.
19. Redondo, R.L., Kim, J., Arons, A.L., Ramirez, S., Liu, X., and Tonegawa, S. (2014). Bidirectional switch of the valence associated with a hippocampal contextual memory engram. Nature *513*, 426–430. https://doi.org/10.1038/nature13725.
20. Lesuis, S.L., Park, S., Hoorn, A., Rashid, A.J., Mocle, A.J., Salter, E.W., Vislavski, S., Gray, M.T., Torelli, A.M., DeCristofaro, A., et al. (2025). Stress disrupts engram ensembles in lateral amygdala to generalize threat memory in mice. Cell *188*, 121–140.e20. https://doi.org/10.1016/j.cell.2024.10.034.
21. Hochgerner, H., Singh, S., Tibi, M., Lin, Z., Skarbianskis, N., Admati, I., Ophir, O., Reinhardt, N., Netser, S., Wagner, S., and Zeisel, A. (2023). Neuronal types in the mouse amygdala and their transcriptional response to fear conditioning. Nat. Neurosci. *26*, 2237–2249. https://doi.org/10.1038/s41593-023-01469-3.

22. Shen, C.-J., Zheng, D., Li, K.X., Yang, J.M., Pan, H.Q., Yu, X.D., Fu, J.Y., Zhu, Y., Sun, Q.X., Tang, M.Y., et al. (2019). Cannabinoid CB1 receptors in the amygdalar cholecystokinin glutamatergic afferents to nucleus accumbens modulate depressive-like behavior. Nat. Med. *25*, 337–349. https://doi.org/10.1038/s41591-018-0299-9.

23. Kim, J., Pignatelli, M., Xu, S., Itohara, S., and Tonegawa, S. (2016). Antagonistic negative and positive neurons of the basolateral amygdala. Nat. Neurosci. *19*, 1636–1646. https://doi.org/10.1038/nn.4414.

24. Campbell, R.R., and Wood, M.A. (2019). How the epigenome integrates information and reshapes the synapse. Nat. Rev. Neurosci. *20*, 133–147. https://doi.org/10.1038/s41583-019-0121-9.

25. Day, J.J., and Sweatt, J.D. (2011). Cognitive neuroepigenetics: a role for epigenetic mechanisms in learning and memory. Neurobiol. Learn. Mem. *96*, 2–12. https://doi.org/10.1016/j.nlm.2010.12.008.

26. Crick, F. (1984). Memory and molecular turnover. Nature *312*, 101. https://doi.org/10.1038/312101a0.

27. Levenson, J.M., O'Riordan, K.J., Brown, K.D., Trinh, M.A., Molfese, D.L., and Sweatt, J.D. (2004). Regulation of histone acetylation during memory formation in the hippocampus. J. Biol. Chem. *279*, 40545–40559. https://doi.org/10.1074/jbc.M402229200.

28. Sweatt, J.D. (2013). The Emerging Field of Neuroepigenetics. Neuron *80*, 624–632. https://doi.org/10.1016/j.neuron.2013.10.023.

29. Collins, B.E., Greer, C.B., Coleman, B.C., and Sweatt, J.D. (2019). Histone H3 lysine K4 methylation and its role in learning and memory. Epigenetics Chromatin *12*, 7. https://doi.org/10.1186/s13072-018-0251-8.

30. Santoni, G., Astori, S., Leleu, M., Glauser, L., Zamora, S.A., Schioppa, M., Tarulli, I., Sandi, C., and Gräff, J. (2024). Chromatin plasticity predetermines neuronal eligibility for memory trace formation. Science *385*, eadg9982. https://doi.org/10.1126/science.adg9982.

31. Oliveira, A.M.M. (2016). DNA methylation: a permissive mark in memory formation and maintenance. Learn. Mem. *23*, 587–593. https://doi.org/10.1101/lm.042739.116.

32. Guo, J.U., Ma, D.K., Mo, H., Ball, M.P., Jang, M.H., Bonaguidi, M.A., Balazer, J.A., Eaves, H.L., Xie, B., Ford, E., et al. (2011). Neuronal activity modifies the DNA methylation landscape in the adult brain. Nat. Neurosci. *14*, 1345–1351. https://doi.org/10.1038/nn.2900.

33. Day, J.J., and Sweatt, J.D. (2010). DNA methylation and memory formation. Nat. Neurosci. *13*, 1319–1323. https://doi.org/10.1038/nn.2666.

34. Halder, R., Hennion, M., Vidal, R.O., Shomroni, O., Rahman, R.U., Rajput, A., Centeno, T.P., van Bebber, F., Capece, V., Garcia Vizcaino, J.C., et al. (2016). DNA methylation changes in plasticity genes accompany the formation and maintenance of memory. Nat. Neurosci. *19*, 102–110. https://doi.org/10.1038/nn.4194.

35. Chen, X., Peng, Y., and Liu, X.S. (2025). DNA Methylation in Long-term Memory. Physiology *40*, 000. https://doi.org/10.1152/physiol.00032.2024.

36. Miller, C.A., and Sweatt, J.D. (2007). Covalent modification of DNA regulates memory formation. Neuron *53*, 857–869. https://doi.org/10.1016/j.neuron.2007.02.022.

37. Lyko, F. (2018). The DNA methyltransferase family: a versatile toolkit for epigenetic regulation. Nat. Rev. Genet. *19*, 81–92. https://doi.org/10.1038/nrg.2017.80.

38. Zhang, X., Zhang, Y., Wang, C., and Wang, X. (2023). TET (Ten-eleven translocation) family proteins: structure, biological functions and applications. Signal Transduct. Target. Ther. *8*, 297. https://doi.org/10.1038/s41392-023-01537-x.

39. Levenson, J.M., Roth, T.L., Lubin, F.D., Miller, C.A., Huang, I.C., Desai, P., Malone, L.M., and Sweatt, J.D. (2006). Evidence that DNA (cytosine-5) methyltransferase regulates synaptic plasticity in the hippocampus. J. Biol. Chem. *281*, 15763–15773. https://doi.org/10.1074/jbc.M511767200.

40. Yu, H., Su, Y., Shin, J., Zhong, C., Guo, J.U., Weng, Y.L., Gao, F., Geschwind, D.H., Coppola, G., Ming, G.l., and Song, H. (2015). Tet3 regulates synaptic transmission and homeostatic plasticity via DNA oxidation and repair. Nat. Neurosci. *18*, 836–843. https://doi.org/10.1038/nn.4008.

41. Meadows, J.P., Guzman-Karlsson, M.C., Phillips, S., Holleman, C., Posey, J.L., Day, J.J., Hablitz, J.J., and Sweatt, J.D. (2015). DNA methylation regulates neuronal glutamatergic synaptic scaling. Sci. Signal. *8*, ra61. https://doi.org/10.1126/scisignal.aab0715.

42. Meadows, J.P., Guzman-Karlsson, M.C., Phillips, S., Brown, J.A., Strange, S.K., Sweatt, J.D., and Hablitz, J.J. (2016). Dynamic DNA methylation regulates neuronal intrinsic membrane excitability. Sci. Signal. *9*, ra83. https://doi.org/10.1126/scisignal.aaf5642.

43. Feng, J., Zhou, Y., Campbell, S.L., Le, T., Li, E., Sweatt, J.D., Silva, A.J., and Fan, G. (2010). Dnmt1 and Dnmt3a maintain DNA methylation and regulate synaptic function in adult forebrain neurons. Nat. Neurosci. *13*, 423–430. https://doi.org/10.1038/nn.2514.

44. Morris, M.J., Adachi, M., Na, E.S., and Monteggia, L.M. (2014). Selective role for DNMT3a in learning and memory. Neurobiol. Learn. Mem. *115*, 30–37. https://doi.org/10.1016/j.nlm.2014.06.005.

45. Gulmez Karaca, K., Kupke, J., Brito, D.V.C., Zeuch, B., Thome, C., Weichenhan, D., Lutsik, P., Plass, C., and Oliveira, A.M.M. (2020). Neuronal ensemble-specific DNA methylation strengthens engram stability. Nat. Commun. *11*, 639. https://doi.org/10.1038/s41467-020-14498-4.

46. Miller, C.A., Gavin, C.F., White, J.A., Parrish, R.R., Honasoge, A., Yancey, C.R., Rivera, I.M., Rubio, M.D., Rumbaugh, G., and Sweatt, J.D. (2010). Cortical DNA methylation maintains remote memory. Nat. Neurosci. *13*, 664–666. https://doi.org/10.1038/nn.2560.

47. Odell, S.C., Taki, F., Klein, S.L., Chen, R.J., Levine, O.B., Skelly, M.J., Nabila, A., Brindley, E., Gal Toth, J., Dündar, F., et al. (2020). Epigenomically Bistable Regions across Neuron-Specific Genes Govern Neuron Eligibility to a Coding Ensemble in the Hippocampus. Cell Rep. *31*, 107789. https://doi.org/10.1016/j.celrep.2020.107789.

48. Lister, R., Mukamel, E.A., Nery, J.R., Urich, M., Puddifoot, C.A., Johnson, N.D., Lucero, J., Huang, Y., Dwork, A.J., Schultz, M.D., et al. (2013). Global epigenomic reconfiguration during mammalian brain development. Science *341*, 1237905. https://doi.org/10.1126/science.1237905.

49. Guo, J.U., Su, Y., Shin, J.H., Shin, J., Li, H., Xie, B., Zhong, C., Hu, S., Le, T., Fan, G., et al. (2014). Distribution, recognition and regulation of non-CpG methylation in the adult mammalian brain. Nat. Neurosci. *17*, 215–222. https://doi.org/10.1038/nn.3607.

50. Kaneda, M., Okano, M., Hata, K., Sado, T., Tsujimoto, N., Li, E., and Sasaki, H. (2004). Essential role for de novo DNA methyltransferase Dnmt3a in paternal and maternal imprinting. Nature *429*, 900–903. https://doi.org/10.1038/nature02633.

51. Trockenbacher, A., Suckow, V., Foerster, J., Winter, J., Krauss, S., Ropers, H.H., Schneider, R., and Schweiger, S. (2001). MID1, mutated in Opitz syndrome, encodes an ubiquitin ligase that targets phosphatase 2A for degradation. Nat. Genet. *29*, 287–294. https://doi.org/10.1038/ng762.

52. Pfirrmann, T., Jandt, E., Ranft, S., Lokapally, A., Neuhaus, H., Perron, M., and Hollemann, T. (2016). Hedgehog-dependent E3-ligase Midline1 regulates ubiquitin-mediated proteasomal degradation of Pax6 during visual system development. Proc. Natl. Acad. Sci. *113*, 10103–10108. https://doi.org/10.1073/pnas.1600770113.

53. Du, H., Huang, Y., Zaghlula, M., Walters, E., Cox, T.C., and Massiah, M.A. (2013). The MID1 E3 Ligase Catalyzes the Polyubiquitination of Alpha4 (α4), a Regulatory Subunit of Protein Phosphatase 2A (PP2A). J. Biol. Chem. *288*, 21341–21350. https://doi.org/10.1074/jbc.M113.481093.

54. Noguchi, S., Arakawa, T., Fukuda, S., Furuno, M., Hasegawa, A., Hori, F., Ishikawa-Kato, S., Kaida, K., Kaiho, A., Kanamori-Katayama, M., et al. (2017). FANTOM5 CAGE profiles of human and mouse samples. Sci. Data *4*, 170112. https://doi.org/10.1038/sdata.2017.112.

55. Hunyara, J.L., and Kolodkin, A.L. (2020). Repurposing developmental mechanisms in the adult nervous system. Curr. Opin. Genet. Dev. *65*, 14–21. https://doi.org/10.1016/j.gde.2020.04.006.

56. Graves, L.A., Heller, E.A., Pack, A.I., and Abel, T. (2003). Sleep deprivation selectively impairs memory consolidation for contextual fear conditioning. Learn. Mem. *10*, 168–176. https://doi.org/10.1101/lm.48803.

57. Cai, D.J., Shuman, T., Harrison, E.M., Sage, J.R., and Anagnostaras, S.G. (2009). Sleep deprivation and Pavlovian fear conditioning. Learn. Mem. *16*, 595–599. https://doi.org/10.1101/lm.1515609.

58. Clark, I.C., Fontanez, K.M., Meltzer, R.H., Xue, Y., Hayford, C., May-Zhang, A., D'Amato, C., Osman, A., Zhang, J.Q., Hettige, P., et al. (2023). Microfluidics-free single-cell genomics with templated emulsification. Nat. Biotechnol. *41*, 1557–1566. https://doi.org/10.1038/s41587-023-01685-z.

59. Kaur, N., Kovner, R., Gulden, F.O., Pletikos, M., Andrijevic, D., Zhu, T., Silbereis, J., Shibata, M., Shibata, A., Liu, Y., et al. (2025). Specification of claustro-amygdalar and palaeocortical neurons and circuits. Nature *638*, 469–478. https://doi.org/10.1038/s41586-024-08361-5.

60. Lim, H., Zhang, Y., Peters, C., Straub, T., Mayer, J.L., and Klein, R. (2024). Genetically- and spatially-defined basolateral amygdala neurons control food consumption and social interaction. Nat. Commun. *15*, 6868. https://doi.org/10.1038/s41467-024-50889-7.

61. Del Boca, C., Lutz, P.E., Le Merrer, J., Koebel, P., and Kieffer, B.L. (2012). Cholecystokinin knock-down in the basolateral amygdala has anxiolytic and antidepressant-like effects in mice. Neuroscience *218*, 185–195. https://doi.org/10.1016/j.neuroscience.2012.05.022.

62. Han, J.H., Kushner, S.A., Yiu, A.P., Cole, C.J., Matynia, A., Brown, R.A., Neve, R.L., Guzowski, J.F., Silva, A.J., and Josselyn, S.A. (2007). Neuronal competition and selection during memory formation. Science *316*, 457–460. https://doi.org/10.1126/science.1139438.

63. Yiu, A.P., Mercaldo, V., Yan, C., Richards, B., Rashid, A.J., Hsiang, H.L.L., Pressey, J., Mahadevan, V., Tran, M.M., Kushner, S.A., et al. (2014). Neurons Are Recruited to a Memory Trace Based on Relative Neuronal Excitability Immediately before Training. Neuron *83*, 722–735. https://doi.org/10.1016/j.neuron.2014.07.017.

64. Pignatelli, M., Ryan, T.J., Roy, D.S., Lovett, C., Smith, L.M., Muralidhar, S., and Tonegawa, S. (2019). Engram Cell Excitability State Determines the Efficacy of Memory Retrieval. Neuron *101*, 274–284.e5. https://doi.org/10.1016/j.neuron.2018.11.029.

65. Choucry, A., Nomoto, M., and Inokuchi, K. (2024). Engram mechanisms of memory linking and identity. Nat. Rev. Neurosci. *25*, 375–392. https://doi.org/10.1038/s41583-024-00814-0.

66. Pappalardi, M.B., Keenan, K., Cockerill, M., Kellner, W.A., Stowell, A., Sherk, C., Wong, K., Pathuri, S., Briand, J., Steidel, M., et al. (2021). Discovery of a first-in-class reversible DNMT1-selective inhibitor with improved tolerability and efficacy in acute myeloid leukemia. Nat. Cancer *2*, 1002–1017.

67. He, Y., and Ecker, J.R. (2015). Non-CG Methylation in the Human Genome. Annu. Rev. Genomics Hum. Genet. *16*, 55–77. https://doi.org/10.1146/annurev-genom-090413-025437.

68. Kupke, J., Klimmt, J., Mudlaff, F., Schwab, M., Lutsik, P., Plass, C., Sticht, C., and Oliveira, A.M.M. (2024). Dnmt3a1 regulates hippocampus-dependent memory via the downstream target Nrp1. Neuropsychopharmacology *49*, 1528–1539. https://doi.org/10.1038/s41386-024-01843-0.

69. Oliveira, A.M.M., Hemstedt, T.J., Freitag, H.E., and Bading, H. (2016). Dnmt3a2: a hub for enhancing cognitive functions. Mol. Psychiatry *21*, 1130–1136. https://doi.org/10.1038/mp.2015.175.

70. Day, J.J., Childs, D., Guzman-Karlsson, M.C., Kibe, M., Moulden, J., Song, E., Tahir, A., and Sweatt, J.D. (2013). DNA methylation regulates associative reward learning. Nat. Neurosci. *16*, 1445–1452. https://doi.org/10.1038/nn.3504.

71. Meroni, G. (1993). MID1-Related Opitz G/BBB Syndrome. In GeneReviews®, M.P. Adam, ed. (University of Washington, Seattle).

72. Yang, Z. (2024). Mid1 deletion leads to cognitive dysfunction in Opitz syndrome by regulates neural rhythms through the inhibition of p-Creb by PP2Ac. eLife *13*, RP103901.

73. Matthes, F., Hettich, M.M., Schilling, J., Flores-Dominguez, D., Blank, N., Wiglenda, T., Buntru, A., Wolf, H., Weber, S., Vorberg, I., et al. (2018). Inhibition of the MID1 protein complex: a novel approach targeting APP protein synthesis. Cell Death Discov. *4*, 4. https://doi.org/10.1038/s41420-017-0003-8.

74. Lu, T., Chen, R., Cox, T.C., Moldrich, R.X., Kurniawan, N., Tan, G., Perry, J.K., Ashworth, A., Bartlett, P.F., Xu, L., et al. (2013). X-linked microtubule-associated protein, Mid1, regulates axon development. Proc. Natl. Acad. Sci. USA *110*, 19131–19136. https://doi.org/10.1073/pnas.1303687110.

75. Liu, E., Knutzen, C.A., Krauss, S., Schweiger, S., and Chiang, G.G. (2011). Control of mTORC1 signaling by the Opitz syndrome protein MID1. Proc. Natl. Acad. Sci. USA *108*, 8680–8685. https://doi.org/10.1073/pnas.1100131108.

76. Koehl, M., Battle, S., and Meerlo, P. (2006). Sex differences in sleep: the response to sleep deprivation and restraint stress in mice. Sleep *29*, 1224–1231. https://doi.org/10.1093/sleep/29.9.1224.

77. Dib, R., Gervais, N.J., and Mongrain, V. (2021). A review of the current state of knowledge on sex differences in sleep and circadian phenotypes in rodents. Neurobiol. Sleep Circadian Rhythms *11*, 100068. https://doi.org/10.1016/j.nbscr.2021.100068.

78. Sripathy, S., Leko, V., Adrianse, R.L., Loe, T., Foss, E.J., Dalrymple, E., Lao, U., Gatbonton-Schwager, T., Carter, K.T., Payer, B., et al. (2017). Screen for reactivation of MeCP2 on the inactive X chromosome identifies the BMP/TGF-β superfamily as a regulator of XIST expression. Proc. Natl. Acad. Sci. *114*, 1619–1624. https://doi.org/10.1073/pnas.1621356114.

79. Cazzulino, A.S., Martinez, R., Tomm, N.K., and Denny, C.A. (2016). Improved specificity of hippocampal memory trace labeling. Hippocampus *26*, 752–762. https://doi.org/10.1002/hipo.22556.

80. Berg, S., Kutra, D., Kroeger, T., Straehle, C.N., Kausler, B.X., Haubold, C., Schiegg, M., Ales, J., Beier, T., Rudy, M., et al. (2019). ilastik: interactive machine learning for (bio)image analysis. Nat. Methods *16*, 1226–1232. https://doi.org/10.1038/s41592-019-0582-9.

81. Stirling, D.R., Swain-Bowden, M.J., Lucas, A.M., Carpenter, A.E., Cimini, B.A., and Goodman, A. (2021). CellProfiler 4: improvements in speed, utility and usability. BMC Bioinf. *22*, 433. https://doi.org/10.1186/s12859-021-04344-9.

82. Pool, A.H., Wang, T., Stafford, D.A., Chance, R.K., Lee, S., Ngai, J., and Oka, Y. (2020). The cellular basis of distinct thirst modalities. Nature *588*, 112–117. https://doi.org/10.1038/s41586-020-2821-8.

83. Liu, H., Zhou, J., Tian, W., Luo, C., Bartlett, A., Aldridge, A., Lucero, J., Osteen, J.K., Nery, J.R., Chen, H., et al. (2021). DNA methylation atlas of the mouse brain at single-cell resolution. Nature *598*, 120–128. https://doi.org/10.1038/s41586-020-03182-8.

84. Cavalcante, R.G., and Sartor, M.A. (2017). annotatr: genomic regions in context. Bioinformatics *33*, 2381–2383. https://doi.org/10.1093/bioinformatics/btx183.

85. Davis, E.S., Mu, W., Lee, S., Dozmorov, M.G., Love, M.I., and Phanstiel, D.H. (2023). matchRanges: generating null hypothesis genomic ranges via covariate-matched sampling. Bioinformatics *39*, btad197. https://doi.org/10.1093/bioinformatics/btad197.

86. Kuleshov, M.V., Jones, M.R., Rouillard, A.D., Fernandez, N.F., Duan, Q., Wang, Z., Koplev, S., Jenkins, S.L., Jagodnik, K.M., Lachmann, A., et al. (2016). Enrichr: a comprehensive gene set enrichment analysis web server 2016 update. Nucleic Acids Res. *44*, W90–W97. https://doi.org/10.1093/nar/gkw377.

87. Fleming, S.J., Chaffin, M.D., Arduini, A., Akkad, A.D., Banks, E., Marioni, J.C., Philippakis, A.A., Ellinor, P.T., and Babadi, M. (2023). Unsupervised removal of systematic background noise from droplet-based single-cell experiments using CellBender. Nat. Methods *20*, 1323–1335. https://doi.org/10.1038/s41592-023-01943-7.

88. Wolock, S.L., Lopez, R., and Klein, A.M. (2019). Computational Identification of Cell Doublets in Single-Cell Transcriptomic Data. Cell Syst. *8*, 281–291.e9. https://doi.org/10.1016/j.cels.2018.11.005.

89. Wolf, F.A., Angerer, P., and Theis, F.J. (2018). SCANPY: large-scale single-cell gene expression data analysis. Genome Biol. *19*, 15. https://doi.org/10.1186/s13059-017-1382-0.

90. Korsunsky, I., Millard, N., Fan, J., Slowikowski, K., Zhang, F., Wei, K., Baglaenko, Y., Brenner, M., Loh, P.R., and Raychaudhuri, S. (2019). Fast, sensitive and accurate integration of single-cell data with Harmony. Nat. Methods *16*, 1289–1296. https://doi.org/10.1038/s41592-019-0619-0.

91. McInnes, L., Healy, J., Saul, N., and Großberger, L. (2018). UMAP: Uniform manifold approximation and projection. J. Open Source Softw. *3*, 861. https://arxiv.org/abs/1802.03426v3.

92. Traag, V.A., Waltman, L., and van Eck, N.J. (2019). From Louvain to Leiden: guaranteeing well-connected communities. Sci. Rep. *9*, 5233. https://doi.org/10.1038/s41598-019-41695-z.

93. Stuart, T., Butler, A., Hoffman, P., Hafemeister, C., Papalexi, E., Mauck, W.M., 3rd, Hao, Y., Stoeckius, M., Smibert, P., and Satija, R. (2019). Comprehensive Integration of Single-Cell Data. Cell *177*, 1888–1902.e21. https://doi.org/10.1016/j.cell.2019.05.031.

STAR★METHODS

KEY RESOURCES TABLE

REAGENT or RESOURCE	SOURCE	IDENTIFIER
Antibodies		
chicken anti-GFP	Aves Labs	Cat# GFP-1020; RRID: AB_10000240
rat anti-*c*-Fos	Synaptic Systems	Cat# 226017; RRID: AB_2864765
Rabbit anti-DNMT3A	Abcam	Cat# 188470; RRID: AB_3073896
Rabbit anti-DNMT1	Abcam	Cat# 188453; RRID: AB_2877711
Guinea Pig anti-NeuN	Synaptic Systems	Cat# 266004; RRID: AB_2619988
rat anti-*c*-Fos	Synaptic Systems	Cat# 226017; RRID: AB_2864765
Bacterial and virus strains		
AAV9-CamKII-GFP-Cre	Addgene	105551-AAV9
AAV9-CMV-GFP-U6-scrmb-shRNA	Vector Biolabs	7045
AAV9-CMV-GFP-U6-*m-Dnmt3a*-shRNA	Vector Biolabs	shAAV-257356
AAV9-CMV-GFP-U6- *m*-Dnmt1-shRNA	Vector Biolabs	shAAV-257355
AAV9-CMV-GFP-U6-m-*Mid1*-shRNA	Vector Biolabs	shAAV-280595
AAV9-EF1A-loxp-scrmb-shRNA-EGFP-loxp-mU6	VectorBuilder	VB251103-1616gps
AAV9-EF1A-loxp- m-*Mid1*-shRNA-EGFP-loxp-mU6	VectorBuilder	VB251103-1619qhm
AAV1-FLEX-tdTomato	Addgene	28306-AAV1
Chemicals, peptides, and recombinant proteins		
4-hydroxytamoxifen (4-OHT)	Millipore Sigma	H6278-10MG
Critical commercial assays		
QIAamp DNA Micro Kit	Qiagen	#56304
Qiagen DNeasy Blood & Tissue Kit	Qiagen	#69504
Pico Methyl-Seq Library Prep Kit	Zymo	#D5455
PIPseq T2 kit	Fluent BioSciences	#FBS-SCR-T2-8-V4.05
Qiagen RNeasy Micro Kit	Qiagen	#74004
Taqman Gene Expression Assay	Applied Biosystems	#4444557
RNAscope Multiplex Fluorescent Detection Kit v2	Advanced Cell Diagnostics	#323110
Deposited data		
Raw sequencing reads (bulk RNA-seq, snRNA-seq, WGBS)	This paper	SRA: PRJNA1304968
WGBS processed data	This paper	GEO: GSE348488, GSE348542, GSE348480
PIPseq processed data	This paper	GEO: GSE348705
Experimental models: Cell lines		
mouse fibroblast	Dr. Antonio Bedalov's lab at University of Washington School of Medicine	NA
Experimental models: Organisms/strains		
C57BL/6J	The Jackson Laboratory	#000664
$Fos^{2A\text{-}iCreERT2}$	The Jackson Laboratory	#030323
CAG-Sun1/sfGFP	The Jackson Laboratory	#021039
$Dnmt3a^{flox/flox}$	Dr. Guoping Fan's lab at UCLA	NA
Software and algorithms		
GraphPad Prism	GraphPad Software	8.4.3
Fiji ImageJ	https://imagej.net/software/fiji/	1.54f

(*Continued on next page*)

Continued

REAGENT or RESOURCE	SOURCE	IDENTIFIER
iLastik	https://www.ilastik.org/	1.3.3post3
CellProfiler	Broad Institute	4.2.5
IMARIS	Oxford Instruments	10
Nikon General Analysis 3	Nikon Instruments Inc	3
ANY-maze behavioral tracking software	Stoelting Co.	7.44
FreezeFrame 5	Actimetrics, Lafayette Instrument	5
PIPseeker	Fluent BioSciences	3.2
Seurat	https://github.com/satijalab/seurat	4.3
Harmony	https://github.com/immunogenomics/harmony	0.0.5
AnnData	https://github.com/scverse/anndata	0.10.8
Scanpy	https://github.com/scverse/scanpy	1.10.3
Scrublet	https://github.com/AllonKleinLab/scrublet	0.2.3
Cellbender	https://github.com/broadinstitute/CellBender	0.2.0
HISAT-3N	https://daehwankimlab.github.io/hisat2/hisat-3n/	NA
ALLCools	https://lhqing.github.io/ALLCools/intro.html	1.0.8
annotatr	https://bioconductor.org/packages/release/bioc/html/annotatr.html	1.34.0
nullranges	https://github.com/nullranges/nullranges	1.12.0
sccomp	https://github.com/MangiolaLaboratory/sccomp	3.22
ClusterGVis	https://github.com/junjunlab/ClusterGVis	0.1.4
enrichR	https://maayanlab.cloud/Enrichr/	3.4

EXPERIMENTAL MODEL AND STUDY PARTICIPANT DETAILS

Animals

All procedures were conducted in accordance with the US National Institute of Health (NIH) guidelines for the care and use of laboratory animals and approved by the Animal Care and Use Committees of Columbia University (Protocol# AC-AABL9550 and #AC-AABF2553). Both male and female adult mice (9–16 weeks old) were used for Figure S1 and only male adult mice were used for all other figures due to the variability of female response to stress and sleep deprivation.[76,77] The following mouse lines were used in the current study: C57BL/6J (JAX 000664), $Fos^{2A\text{-}iCreERT2}$ (TRAP2; JAX 030323), CAG-Sun1/sfGFP (JAX 021039), $Dnmt3a^{flox/flox}$ (Dr. Guoping Fan at UCLA). Mice were housed in 12-h light-dark cycles (lights on at 07:00 a.m. and off at 07:00 p.m., temperatures of 65–75°F with 40–60% humidity) with free access to food and water. Behavioral testing was performed during the light phase.

Cell lines

Mouse fibroblasts were kindly provided by Dr. Antonio Bedalov[78] and were cultured in Dulbecco's Modified Eagle Medium (DMEM; Gibco) supplemented with Cosmic Calf Serum (Hyclone), L-glutamine (Gibco), non-essential amino acids (Gibco), and penicillin-streptomycin (Gibco). Cells were maintained at 37°C in a humidified incubator with 5% CO_2. Cell identity was confirmed by genotyping. Mycoplasma contamination was assessed using the E-Myco Plus kit (Bulldog Bio#25234), and all cultures were confirmed to be negative for mycoplasma contamination.

METHOD DETAILS

Viral injection

Mice were anesthetized with a mixture of ketamine and Xylazine (100 and 10 mg kg^{-1}, intraperitoneally), then placed on a stereotaxic frame with a closed-loop heating system to maintain body temperature. After asepsis, the skin was incised to expose the skull and a small craniotomy (~0.5 mm in diameter) was made on the skull above the regions of interest. A solution containing 50–200 nL (~$1X10^{13}$ GC/mL) AAV virus was loaded into a pulled glass capillary and injected into the BLA bilaterally (AP -1.45mm, ML 3.4mm, DV -5.0mm) using a Nanoinjector (WPI). The DV Coordinates listed above are relative to the bregma surface. After surgery, the animals returned to home-cage to recover for at least two weeks (with exception of the 3-day post-surgery training in *Dnmts* and *Mid1* shRNA knockdown experiment) before any experiment.

Animal behavior

Contextual and auditory fear conditioning

Both contextual and auditory fear conditioning training sessions were conducted in conditioning chambers (Coulbourn Instruments) featuring a transparent plastic front door, a rear wall with a checkerboard pattern, stainless steel side panels, and a metal grid floor. A house light was mounted on the left interior wall. Each chamber was enclosed within a sound- and light-attenuating plastic cabinet equipped with continuous ventilation provided by a running fan. A paper towel dabbed with 550ul lemon solution (1:50) was placed beneath the metal grid to provide a distinct olfactory cue. Mice were transported to the testing apparatus in standard home cages. Between sessions, chambers were sanitized with 70% ethanol followed by Milli-Q water, thoroughly dried, and allowed to ventilate for 5 min prior to the next trial.

All training sessions were conducted over a total duration of 450 s. During the auditory fear conditioning (aFC), mice were exposed to visual/olfactory context and three auditory tone stimuli (80 dB, 2kHz, 30s each), which co-terminated with foot shocks (0.5–1.0 mA, 2s) delivered at 150s, 270s, and 390s into the session. During the contextual fear conditioning (cFC), only visual/olfactory contextual cues were applied and the auditory tone stimuli was not given.

For contextual fear recall (cFR), mice were returned to the original conditioning chamber and allowed to freely explore for a total of 5 min, during which no tones or shocks were presented. For auditory fear recall (aFR), mice were placed in a novel context and exposed to three tone presentations (80 dB, 2kHz, 3 min each) at the 3rd, 9th, and 15th minutes of an 18-min session. Each tone was separated by a 3-min interval without any stimuli. The novel context was a modified version of the original fear conditioning (FC) chamber. The metal grid floor was covered with a yellow plastic insert, and the walls were lined with blue plastic sheets to alter the chamber's shape into a cylindrical configuration. Bedding was added to the floor. Unlike the conditioning context, no scent was used. The room was dimly lit, and mice were transported to the apparatus in a white bucket.

Sleep deprivation (SD)

A day prior to FC and SD experiment, mice were placed in the SD chamber for 1hr to acclimate to it. Immediately following fear conditioning training on the next day, mice assigned to the sleep deprivation (SD) group were placed into SD chambers equipped with automated treadmills at 2cm/s speed, programmed to operate in 5-s on/10-s off cycles, which forced animals to move every 10 s. Each chamber accommodated a maximum of two mice to ensure adequate space and consistent stimulation. Sleep deprivation was maintained continuously for 24 h. Upon completion of the deprivation period, mice were returned to their respective home cages for at least 72-h recovery period. Mice in the SD and control groups were housed separately throughout the FC-SD protocol to prevent potential social buffering or disturbance effects.

Open field test (OFT)

Open field testing was conducted in a square chamber measuring 16 × 16 inches with a height of 12 inches. The chamber was cleaned before and after each trial using 70% ethanol followed by Milli-Q water and then wiped dry with a clean towel to eliminate olfactory cues. Mice were placed in the behavior room prior to OFT to allow adjustment to its lighting and ambient noise conditions. Light intensity within the open field arena was maintained consistently at 100–120 lux throughout the experiment and measured using a digital light lux meter. At the beginning of each trial, a video recording was initiated for a few frames with the empty arena. A single mouse was then gently transferred to the center of the chamber. Behavior was recorded for 10 min. At the end of the session, the mouse was returned to its home cage, and the number of fecal boli produced during the trial was recorded as an indicator of emotional reactivity. The arena was subsequently sanitized with 70% ethanol followed by Milli-Q water, thoroughly dried, and allowed to ventilate for 5 min prior to the next trial. Pre-recorded OF videos were automatically scored using ANY-maze behavioral tracking software (Stoelting, Wood Dale, IL, v7.44). Based on the dimension of the OF (400 mm × 400 mm), the arena was divided into an evenly-spaced 5 x 5 grid (80 mm × 80 mm per square). The center of the arena was defined as the centermost 3 x 3 grid and the periphery was defined as the outermost remaining squares. Number of entries, duration time, and overall distance travel were quantified in 60 s time bins.

TRAP2;Sun1-GFP mice behavioral timeline

To minimize nonspecific activity-dependent labeling in TRAP2;Sun1-GFP mice, animals were transferred to a dark environment (with *Ad libitum* water and food) starting at least 12h before 4-hydroxytamoxifen (4-OHT) injection and remained in darkness for 72 h following 4-OHT, including sleep deprivation.[79] Contextual fear conditioning (cFC) was the only paradigm with light on in the chamber.

On the day of labeling, 4-OHT was administered at 09:00 (ZT2). CFC was performed at 14:00 (ZT7) (the noFC group experienced context-only exposure by being placed in the cFC chamber for the same duration without shock). Mice were then immediately subjected to 24 h of SD (14:00–14:00 the next day; ZT7–ZT7) (noSD group was placed in the SD chamber without treadmill turning on). After completion of SD, mice were returned to their home cage (still in darkness) for the remainder of the 72 h post-4-OHT dark period. Three days after 4-OHT, animals were transferred back to the standard animal facility and re-exposed to the normal light-dark cycle.

Histology, immunohistochemistry, and cell counting

In TRAP2; Sun1-GFP double labeling experiment, mice were perfused 1.5hr after fear recall using PBS followed by 4% paraformaldehyde (PFA), and brains were fixed with PFA for 1 day at 4°C. Brains were sectioned coronally at 100um and processed for

immunostaining. Slices were blocked and permeabilized with PBS containing 5% heat inactivated donkey serum and 0.3% Triton X-100 at 4C for 1hr and then incubated with anti-GFP (chicken, Aves Labs, Cat#GFP-1020, 1:1000) and c-Fos antibody (rat, Synaptic Systems, cat#226017, 1:1000) at 4C overnight. Slices were incubated with anti-chicken Alexa 488 (donkey, Jackson ImmunoResearch, Cat#703–545-155, 1:500) and anti-rat Alexa 594 (donkey, Jackson ImmunoResearch, cat#712–585-153, 1:500) at 4°C overnight. Tissue sections were mounted on microscope glass slides and imaged using a Yokogawa CSU-W1 spinning disk confocal microscope mounted on a Nikon Ti2-E stand using a 10x (BLA) 20× (Hippocampal subregions) NA Plan Apochromat objective (Nikon Instruments Inc). Image processing and quantification were performed using Nikon NIS-Elements, NIS.ai (Artificial Intelligence) and Nikon General Analysis 3 (GA3) software package (Nikon Instruments Inc). The neural network was trained using a set of manually annotated c-Fos positive cells images, including training datasets specifically created for hippocampal subregions and BLA to account for their unique cellular and structural characteristics. Segment.ai was then applied to identify and segment c-Fos positive cells and it was included in a NIS GA3 workflow to be able to identify and segment the signal from the different channels and quantify the ''co-labelled'' cells.

For immunostaining of DNMT3A and DNMT1, 4% PFA-fixed mouse brains were cryoprotected by sequential immersion in sucrose solutions (20%–30% sucrose). Following sucrose infiltration, brains were embedded in OCT and stored at −80°C until sectioning. Upon sectioning, coronal brain sections were cut at a thickness of 40 μm using cryostat (Leica#CM3050) and collected into a 48-well plate containing 1X PBS. Sections were then washed in 1X TBS (145mM NaCl, 5mM Tris-HCL, pH = 7.4) for 3 times with 10 min each. Antigen retrieval was performed via heating sections at 70°C for 40 min in 1X HistoVT solution (Fisher Scientific#NC0499519), followed by another 3 washes of 1X TBS. Sections were blocked and permeabilized with TBS containing 5% heat inactivated donkey serum and 0.3% Triton X-100 at 4C for 1hr then incubated anti-NeuN (guinea pig, Synaptic Systems, Cat#266004, 1:1000), anti-DNMT3a (rabbit, Abcam, #188470, 1:200) or anti-DNMT1 (rabbit, Abcam, #188453, 1:500) at 4°C overnight. For secondary antibody, sections were incubated with anti-rabbit Alexa 488 (donkey, Jackson ImmunoResearch, Cat# 711–545-152, 1:500) or anti-rabbit Alexa 594 (donkey, Jackson ImmunoResearch, Cat#711–585-152, 1:500), and anti-guinea pig Alexa 674 (donkey, Jackson ImmunoResearch, cat# 706–605-148, 1:500) at 4°C overnight. Tissue sections were mounted on microscope glass slides and imaged.

For counting the number of AAV-Cre infected cells expressing DNMT3A in Figure S1B, quantification was performed using sections from a single animal per group, as representative confirmation of recombination efficiency and a validation consistent with prior publications using this line.[50] fluorescence images were acquired on a Zeiss LSM 800 confocal microscope at 20× with channels corresponding to NeuN (Alexa Fluor 647) and DNMT3A (Alexa Fluor 594). Each channel was split in Fiji (ImageJ, v1.54f) and loaded into CellProfiler (v4.2.5) to identify GFP-positive cells (virus infected cells) and DNMT3A -positive cells. RelateObject module was used to calculate the number of GFP-positive cells expressing DNMT3A.

In Figure S1D, to validate the DNMT3A knockdown in TRAP2;*Dnmt3a*$^{fl/fl}$ mice using the intensity level of DNMT3A expression, z stack fluorescence images were acquired on a Nikon W1 spinning disk confocal microscope at 20x with channels corresponding to NeuN (Alexa Fluor 647), tdTomato, and DNMT3A (Alexa Fluor 488). In Figures 1A and 1B, also to quantify DNMT3A expression intensity, z stack fluorescence images were acquired on a Zeiss LSM 800 confocal microscope at 40× with channels corresponding to NeuN (Alexa Fluor 647) and DNMT3A (Alexa Fluor 488). Next, raw.nd2 files (or.czi files) were processed in Fiji (ImageJ, v1.54f) using the Bio-Formats importer, with maximum intensity projections generated for Figure S1D to maximize detection of tdTomato-labeled cell bodies for downstream segmentation, and average intensity projections for Figures 1A and 1B to reduce the contribution of out-of-focus signal to DNMT3A intensity measurements. In both cases, individual fluorescence channels were extracted and saved as separate TIFF files. For Figure S1D, tdTomato channel images were imported into ilastik (v1.3.3) for pixel classification using a random forest model to distinguish cell bodies from projections and background, generating grayscale probability maps indicating per-pixel cell likelihood[80]; these probability maps together with DNMT3A and NeuN channel images were then loaded into CellProfiler (v4.2.5) to measure DNMT3A expression intensity in tdTomato-positive and -negative cells.[81] For Figures 1A and 1B, NeuN and DNMT3A TIFF files were loaded directly into CellProfiler (v4.2.5) to quantify DNMT3A intensity within NeuN-positive cells. For all quantifications, cell-level measurements exported from CellProfiler were compiled and statistical comparisons were performed in GraphPad Prism (v8.4.3).

Tissue preparation for WGBS and PIP-seq

Mice were subject to contextual fear recall and euthanized immediately (WGBS) or 1 h after (PIP-seq). All tissue preparation steps were performed in an RNase-free environment. The perfusion and slicing platforms were set up in advance, and the vibratome cutting chamber was surrounded with crushed ice and dry ice to maintain low temperature throughout. NMDG-HEPES artificial cerebrospinal fluid (ACSF) was prepared fresh and carbogenated (93 mM NMDG, 2.5 mM KCl, 1.2 mM NaH_2PO_4, 30 mM $NaHCO_3$, 20 mM HEPES, 25 mM glucose, 10 mM $MgSO_4$, 1 mM $CaCl_2$, 1 mM kynurenic-acid Na salt, 5 mM Na-ascorbate, 2 mM thiourea and 3 mM Na-pyruvate, pH adjusted to 7.4, osmolarity is around 300–310 mOsm) on ice prior to use.[82] Mice were anesthetized with isoflurane, and brains were rapidly extracted and immersed in ice-cold, carbogenated NMDG-HEPES-ACSF. Brains were sectioned coronally at 300 μm thickness using a vibratome (Leica VT1200S) in ice-cold, carbogenated NMDG-HEPES-ACSF. Sections were transferred to a chilled, oxygenated chamber containing the same ACSF. For microdissection of the BLA, individual slices were transferred to a clean dissection dish containing ice-cold NMDG-HEPES-ACSF supplemented with 30 μM actinomycin D. The dissection dish was placed on a pre-chilled metal block to maintain low temperature throughout the procedure. Micro-dissected BLA tissue was

immediately transferred into Protein LoBind tubes (Eppendorf) containing 50 μL of NMDG-HEPES-ACSF–ActD supplemented with 0.2 U/μL RNase inhibitor (Takara Bio). Following collection, tissue samples were flash-frozen in liquid nitrogen and stored at −80°C until further processing.

Nuclei isolation

Nuclei were isolated using a modified EZ PREP-based protocol optimized to minimize mechanical damage and doublet formation. All steps were performed on ice or at 4°C, and care was taken to avoid bubble formation or unnecessary agitation. A swinging bucket centrifuge and all tools, including a Dounce homogenizer and pestles (Sigma #D8938), were pre-chilled on ice. Brain tissue was transferred into EZ PREP buffer (Thermo Fisher, contained in Nuc-101), using 0.5 mL per mouse, and homogenized in a 1.5 mL Dounce homogenizer with 25 strokes each using pestles A and B. Following homogenization, the lysate was transferred to a pre-chilled 2 mL LoBind tube wrapped in aluminum foil to protect fluorescent signals and incubated on ice for 5 min. The homogenate was centrifuged at 500 × g for 5 min at 4°C, washed once in 1 mL cold EZ PREP buffer, and pelleted again under the same conditions. The final pellet was resuspended in 1 mL of staining buffer composed of 1× PBS with 0.5% BSA and 0.2 U/μL RNase inhibitor. After a final wash, nuclei were resuspended in 0.5 mL staining buffer for FANS.

Fluorescence-activated nuclear sorting (FANS)

Immediately prior to sorting, nuclei suspensions were gently triturated using pipette tips pre-coated with staining buffer and filtered through a 40 μm cell strainer into pre-wet 1.5 mL Protein LoBind tubes. To aid in debris discrimination and viability gating, 0.5 μL of DRAQ5 DNA dye (BioLegend #424101) was added to each sample. Flow cytometry was performed using a Sony SH800 sorter equipped with a 100 μm nozzle. Single-nuclei events were first gated based on forward scatter (FSC-A) vs. back scatter (BSC-A). Doublets and aggregates were then excluded based on DRAQ5-H vs. DRAQ5-A gating. Finally, Sun1-GFP-positive nuclei were selected based on GFP signal vs. DRAQ5-A intensity.

For genomic DNA extraction from sorted nuclei, lysis buffer was prepared in advance by combining 100 μL ATL buffer with 10 μL Proteinase K (both from the QIAamp DNA Micro kit, Cat#56304) in a 1.5 mL DNA LoBind tube (Eppendorf). This lysis mix was added to each tube prior to sorting and kept at room temperature. During flow cytometry, sorted nuclei were collected directly into the prepared lysis buffer. Following sorting, AL buffer (Qiagen) was added at a 1:1 volume ratio relative to ATL to facilitate complete lysis. Samples were then processed for DNA purification following the manufacturer's protocol.

For single nuclei RNA sequencing via PIPseq, sorted nuclei were collected into 185 μL of cold Nuclei Suspension Buffer per ∼5,000 events (typically 15 μL of 1:1 tube of GFP+ and 3 tubes of GFP– from combined BLA regions). Sorting was performed at a low pressure (4 PSI) to preserve nuclear integrity. After sorting, tubes were centrifuged at 500 × g for 5 min at 4°C. Post-spin, approximately 186 μL of supernatant was carefully removed (for ∼2,000 sorted nuclei) without disturbing the loosely packed nuclear pellet. To do this with precision, a P200 pipette was first used to bring the tip of the supernatant close to the bottom, followed by a P10 pipette to gently remove the final 4 μL of the supernatant, ensuring nuclei pellet to be not disturbed. The remaining nuclei (∼5 μL of pellet) were resuspended by gentle pipetting using low-retention tips and 4ul were transferred to a thawed PIPs tube (Fluent BioSciences). To each tube, 0.5 μL of 40 U/μL RNase inhibitor (Takara Bio) was added directly into the same tube. Samples were then immediately processed for RNA extraction and library preparation following the PIPseq T2 Protocol (Fluent BioSciences).

Whole-genome bisulfite sequencing (WGBS)

Genomic DNA was extracted from BLA sorted nuclei using QIAamp DNA Micro kit (Qiagen #56304) with RNase kit (Qiagen #19101), following the manufacturer's protocol. The integrity and concentration of the gDNA were assessed using 1XdsDNA HS Qubit Assay and Qubit fluorometer.

The WGBS library was prepared using Pico Methyl-Seq Library Prep Kit (Zymo #D5455) which is designed for ultra-low DNA input amount. 1-100ng of high-quality gDNA was first bisulfite converted using the kit's Lightning Conversion Reagent, converting unmethylated cytosines to uracils while leaving methylated cytosines unchanged. DNA was also fragmented at this step. Post-conversion, DNA was desulphonated and purified using Zymo-Spin IC Columns, ensuring the removal of the bisulfite salts and other contaminants. Then DNA was subjected to random priming and pre-amplification using the PrepAmp reagents, generating a library of DNA fragments suitable for sequencing. Then these amplified libraries were further enriched using the LibraryAmp Master Mix and indexed with the provided Index Primer Sets, enabling multiplexed sequencing. Lastly, the libraries were purified to remove residual primers, enzymes, and reaction components for high-quality libraries ready for sequencing. Library quality and concentration were evaluated using Agilent TapeStation systems and Qubit fluorometer respectively.

The sequencing was performed on an Illumina NovaSeq 6000 to generate 150 bp paired end reads. Raw sequencing data were initially assessed using FastQC to evaluate base quality scores, adapter contamination, and other quality metrics. Trimming was performed using cutadapt (v 4.9) with the following parameters: adapter sequences (-a AGATCGGAAGAGCACACGTCTGAAC for read 1, -A AGATCGGAAGAGCGTCGTGTAGGGA for read 2), a quality cutoff of Q20 (-q 20), fixed trimming of 10 bases from the 5′ end and 15–20 bases from the 3′ end of both reads (-u 10 -u −15 -U 10 -U −20), and a minimum length requirement of 30 bp for both reads (-m 30:30). Only read pairs passing the quality and length thresholds for both mates were retained (–pair-filter both). Trimmed reads were compressed and saved in a dedicated directory. Cleaned reads were then aligned to the mouse reference genome (mm10) using HISAT-3N (https://daehwankimlab.github.io/hisat2/hisat-3n/). PCR duplicates were identified and removed using Picard's

MarkDuplicates (Picard v 2.27.5; Samtools v 1.20). All downstream methylation calling and ALLCools (v 1.0.8) analysis were performed using deduplicated BAM files. Comprehensive quality control and alignment statistics are provided in Table S1. All downstream methylation calling and ALLCools analysis were performed on deduplicated BAMs.

After alignment and PCR duplicate removal, BAM files were converted to ALLC format using ALLCools.[83] To enable context-specific methylation analysis, cytosine methylation calls were extracted by context (e.g., mCG) using the extract-allc module of ALLCools. Output files were saved in a context-specific directory structure (e.g., allc-CGN). Each sample was processed individually to produce strand-merged, context-filtered ALLC files suitable for input into subsequent ALLCools modules. These ALLC files were then converted to BigWig format using ALLCools to enable visualization of cytosine methylation levels across the genome. For differential analysis, ALLC files were grouped by behavioral condition and merged using merge_allc. Differentially methylated sites (DMS) were identified using the call_dms function with the following parameters: max_row_count = 50, n_permute = 3000, min_pvalue = 0.01, and cpu = 8. Subsequent DMR (differentially methylated region) calling was performed with call_dmr, using the filtered DMS as input and the following thresholds: p_value_cutoff = 0.05, frac_delta_cutoff = 0.3, max_dist = 250, residual_quantile = 0.7, and corr_cutoff = 0.3. All analyses were performed using the mm10 mouse genome assembly and the associated chromosome size file. AllCools DMR calling generated methylation difference between pairwise comparison in the representation of −1 to 0 for hypomethylation and 0 to 1 for hypermethylation. The density of methylation difference was smoothed histogram generated by geom_density function in R.

DMR genomic regions annotations and enrichment

DMRs were annotated via annotatr package and its annotation include: 1 to 5Kb upstream of the TSS, promoter (less than 1Kb upstream of the TSS), 5′UTR, first exons, exons, introns, intron-exon boundaries, exon-intron boundaries (200bp up/downstream of any boundary between and exon and an intron), CDS, 3′UTR, intergenic regions (the intergenic regions exclude the previous list of annotations), FANTOM5 permissive enhancers, GENCODE lncRNA, and CpG annotations, which include shores (2Kb upstream/downstream of the ends of the CpG islands (CGI), shelves (another 2Kb upstream/downstream of the farthest upstream/downstream limits of the CpG shores), inside islands, and inter CGI).[84]

To assess whether the observed DMR enrichments in genomic features were greater than expected by chance, we first generated randomized DMR sets using the randomizeRegions() function from the annotatr wrapper with 100 iterations to generate a large pool of candidate null regions that match the real DMRs in number, size, and chromosomal distribution. Second, we scored both real DMRs and candidate null regions for three genomic properties: CpG density, GC content, and gene density. These scores were computed from the mm10 genome sequence and gene annotation. Next, we used matchRanges() from the nullranges package[85] to select, from the large candidate pool, a final set of null regions that closely match the real DMRs on all three properties. The enrichment analysis was then assessed by comparing the proportion of real DMRs overlapping each annotation category against a matched null distribution using Fisher's exact test, with Benjamini-Hochberg (BH) correction for multiple comparisons across annotation categories. Annotations with BH-adjusted $p < 0.05$ were considered significantly enriched or depleted.

DMGs pathway enrichment analysis

The pathway analysis was performed using the enrichR R package[86] against GO Biological Process 2025. EnrichR uses its own internally curated background by default, which is based on all genes present in the selected databases.

DMRs overlap with pairwise comparisons

Pairwise overlaps between DMR sets were computed using bedtools intersect, requiring a minimum of 1 bp overlap. The methylation direction is based on the sign of methylation change. For each pair of DMR sets, Jaccard Index was computed to quantify the shared DMRs (sDMRs) using the formular:

$$Jaccard\ Index = \frac{|A \cap B|}{|A \cup B|}$$

|A∩B| is the number of shared DMRs, and |A∪B| is the total number of unique DMRs across the two sets (excluding duplicates). Jaccard indices were calculated for DMRs with same and opposite methylation direction. The chord diagrams were generated using the circlize R package (v0.4.15) to visualize the pairwise overlaps between DMR sets. For each group comparison, the width of its chords (edges) was set proportional to the sum of its Jaccard indices with all other comparisons, representing the total proportion of shared DMRs. To evaluate whether observed DMR overlaps exceeded random expectation, empirical permutation tests were performed. One of the DMR sets in each pair was shuffled 1,000 times using bedtools shuffle with constraints to preserve chromosomal distribution and length in the universe of all same context DMRs. In each random shuffle of DMR set A, the number of overlaps in base pairs overlapped with DMR set B was recorded, which is used to generate a null distribution. The empirical p-value was calculated as:

$$p = \frac{\#(random\ overlaps \geq observed\ overlap) + 1}{number\ of\ iterations + 1}$$

In addition, the fold enrichment (observed overlapped base pairs over expected overlapped base pairs from overlapping DMR set B to a random shuffle of DMR set A) is documented together with the p values, see Table S2.

DNA methylation reversal score within shared DMRs (sDMRs)

To quantify the degree to which sleep deprivation after fear conditioning (FC-SD) disrupted the methylation changes induced by fear conditioning with sleep (FC-Sleep), we computed a per-sDMR reversal score (R) for sDMRs identified at the intersection of the FC-Sleep vs. noFC-Sleep and FC-SD vs. FC-Sleep comparisons. For each sDMR, group mean CG or CH methylation levels were calculated across three conditions: the context-only sleep control (noFC-Sleep), the fear conditioning with sleep group (FC-Sleep), and the fear conditioning with sleep deprivation group (FC-SD). The reversal score (R) is calculated as, where Met represents the group mean methylation:

$$R = 1 - \frac{Met(FCSD) - Met(noFCSleep)}{Met(FCSleep) - Met(noFCSleep)}$$

Using R, we classified the DMR as showing strong reversal ($R \geq 0.75$), partial reversal ($0.25 \leq R < 0.75$), or minor reversal ($R < 0.25$). DMRs were excluded from reversal scoring if (1) the FC-induced methylation effect was below a minimum threshold of 2% absolute methylation difference, as a near-zero difference renders the ratio numerically unstable and biologically uninterpretable; (2) $R < 0$ due to minor signal shifts introduced by the union-based coordinate merging.

PIPseq for single nuclei RNA sequencing

RNA was extracted and its sequencing library was prepared using the PIPseq T2 kit (Fluent BioSciences, Cat. # FBS-SCR-T2-8-V4.05), following the manufacturer's protocol. Briefly, single nuclei RNA was captured using PIPs and proceeded to cDNA synthesis, amplification, and isolation. After examining the cDNA quantity and quality using Agilent TapeStation and Qubit flurometer respectively, cDNA was proceeded with fragmentation, end repair, A-Tailing, adapter ligation, and sample barcoded with P7 and P5 index primers for multiplexing, followed by clean-up.

Read 1 captured cell barcode and unique molecular identifier (UMI) information, while Read 2 contained gene expression sequences. Libraries were sequenced on Illumina NovaSeq X Plus to generate 150 bp paired end reads.

Processing PIP-seq data and initial quality control

PIPseeker (v 3.2) was used to map PIP-seq reads to the reference transcriptome (mm10) to quantify gene expression in single nuclei from each sample (parameters chemistry = v4 for the first batch and chemistry = v5 for the second batch). Ambient RNA signal, which can add considerable noise to single-cell transcriptomics data, was identified and corrected using Cellbender[87] remove-background (v 0.2.0). The likelihood of a droplet containing more than one cell for all cells in each sample were then computed using Scrublet[88] (v 0.2.3) with default settings. Each sample was individually loaded into Scanpy[89] (v 1.10.3) and the samples were concatenated into a single AnnData (v 0.10.8) object. We removed barcodes that were in the top 2.5% of the number of UMIs, percentage of mitochondrial counts, and doublet probability for each sample.

Dimensionality reduction, clustering, and additional filtering

The UMI counts matrix was normalized for each cell by the total UMI counts in all genes, and log transformed using the Scanpy functions sc.pp.normalize_total and sc.pp.log1p respectively. Highly variable genes (HVGs) were identified using the Scanpy function sc.pp.highly_variable_genes, and the data matrix comprising these HVGs were scaled to unit variance and centered at zero mean using the sc.pp.scale function. We performed principal component analysis (PCA) in this scaled data matrix using the sc.tl.pca function, yielding a linear dimensionality reduction of the snRNA-seq dataset. PCs were corrected for technical variation from sequencing batches using the Harmony[90] algorithm in the harmonypy package (v 0.0.5). The top 30 harmonized PCs were used to construct a neighborhood graph of the nuclei using the sc.pp.neighbors function with a cosine distance metric and n_neighbors = 15. A two-dimensional representation of the data was then computed on this neighborhood graph using the uniform manifold approximation and projection[91] (UMAP) algorithm with the Scanpy function sc.tl.umap. We performed an initial clustering analysis grouping nuclei into clusters in the same neighborhood graph representation using the Leiden[92] algorithm with the function sc.tl.leiden and a resolution parameter of 2.0. Leiden clusters were organized hierarchically by similar expression profiles using the function sc.tl.dendrogram.

We next performed a sub-clustering analysis containing only neuronal cell types. We inspected the expression of canonical cell-type markers in each Leiden cluster to annotate broad cell types, and we noted that several Leiden clusters displayed conflicting marker gene expressions. Further, we inspected the distributions of QC metrics in each Leiden cluster and determined that several clusters were outliers in these metrics, and we removed these low-quality clusters. The final processed dataset consisted of 12,183 (5,632 from first batch and 6,511 from second batch) neurons.

Differential gene expression analysis

Differential expression analysis was performed in Seurat[93] (v 4.3) using the 'FindMarkers' function (parameters logfc.threshold = 0.1, test.use = ''wilcox'', min.pct = 0). We pooled the DEGs (meeting adjusted $p < 0.05$ and abs(avg_log2FC) > 0.3 from pairwise comparisons together and performed clustering and visualization using ClusterGVis (https://github.com/junjunlab/ClusterGVis) with Mfuzz method.

Single cell proportion test

We use sccomp (v3.22) to calculate the proportional difference in cell number proportions between clusters in PIP-seq.

Bulk RNA sequencing

Total RNA was extracted from flash frozen and micro-dissected BLA using Qiagen RNeasy Micro Kit (Qiagen #74004), with extra DNase I digestion on the column, following the manufacturer's instructions. The extracted RNA samples were submitted to Novogene Corporation (Sacramento, CA) for library preparation, sequencing, and analysis. RNA integrity was assessed using the Agilent 5400 Fragment Analyzer, and samples with RNA Integrity Number (RIN) values $\geq$ 7.0 were selected for poly(A) enrichment library preparation and sequencing by Novogene. The sequencing was conducted on an Illumina NovaSeq X Plus platform, generating 150 bp paired-end reads.

qRT-PCR

Total RNA was extracted from flash frozen and micro-dissected BLA using Qiagen RNeasy Micro Kit (Qiagen #74004), with extra DNase I digestion on the column, following the manufacturer's instructions. RNA was transcribed into cDNA using the Vazyme HiScript III RT SuperMix (#R323-01; Vazyme, Nanjing, PRC). The thermal cycling was conducted with 15 min of 37°C followed by 1 min of 85°C, then held at 4°C. qRT-PCR was performed on QuantStudio™ 3 Real-Time PCR System (Applied Biosystems, Foster City, CA, USA) using TaqMan fast advanced gene expression assays(#4444557; Applied Biosystems, Foster City, CA, USA). The following TaqMan gene expression assays were used: *Mid1* (Mm04933166_m1) and the housekeeping gene *Gusb* (Mm00446953_m1). 2 μL of diluted cDNA (about 20 ng) was added to each reaction. The thermal cycling was conducted with the following settings: a 2 min incubation at 50°C, 20 s at 95°C, followed by 40 cycles of 1 s each at 95°C, 20 s at 60°C. Relative expression levels of each target transcript were determined by the ΔΔCt method using Gusb mRNA levels as a reference.

RNAscope for validating *Mid1* knockdown

To quantify *Mid1* mRNA levels in individual neurons within the BLA of C57 mice injected with AAV-shRNA targeting *Mid1* or AAV-scrRNA (12 weeks old, n = 3 per group), fluorescence *in situ* hybridization (FISH) was performed using the RNAscope Multiplex Fluorescent Detection Kit v2 (Advanced Cell Diagnostics, #323110) according to the manufacturer's instructions. Two RNAscope probes were used to detect *Mid1* and EGFP: *Mid1* probe (Advanced Cell Diagnostics, #518101), and EGFP probe (Advanced Cell Diagnostics, #400218-C2). Mice were perfused with 4% paraformaldehyde (PFA; Fisher Scientific, #AAJ19943K2) in PBS, and brains were post-fixed overnight in 4% PFA at 4°C. Then washed in PBS and cryoprotected in a graded sucrose series (10% overnight, 20% overnight, and 30% sucrose in 1x PBS overnight) at 4°C prior to processing. Brains were snap-frozen in powdered dry ice and then cryoprotected in OCT embedding medium (Thermo Fisher). Mouse brains were sectioned coronally at 100 μm. After washing in PBS, sections were post-fixed in 4% PFA for 1 h, followed by treatment with hydrogen peroxide (Advanced Cell Diagnostics, #323110), target retrieval reagent (Advanced Cell Diagnostics, #322000), and protease digestion (Protease III, Advanced Cell Diagnostics, #322337). *Mid1* and EGFP RNAscope probes were hybridized for 2 h. Signal amplification was performed using HRP, followed by fluorescent labeling with Opal 520 (Akoya Biosciences, #OP-001001) for EGFP and Opal 570 (Akoya Biosciences, #OP-001003) for *Mid1*. Fluorescent dyes were diluted 1:1000 in TSA buffer (Advanced Cell Diagnostics, #322810). Between steps, sections were washed with RNAscope washing buffer (Advanced Cell Diagnostics, #310091) as instructed. Brain sections were mounted using Fluoro-Gel II with DAPI (Electron Microscopy Sciences, #1798551). Images were acquired using a Zeiss LSM 810 confocal microscope: whole-brain images were captured using a 10× objective with tile scanning, and high-resolution images of individual neurons were captured with a 40× objective and z stack acquisition. z stack images were deconvolved using IMARIS 10 (Oxford Instruments) to improve clarity. The Extended Depth of Field (EDF) plugin (Biomedical Imaging Group) in ImageJ (FIJI) was used to merge Z-stacks into a single in-focus image. For *Mid1* mRNA quantification, GFP-positive, non-overlapping neurons in the BLA were selected, and fluorescent particles within their somata were counted. Regions of interest (ROIs) were manually drawn in ImageJ (FIJI). Background noise was reduced using thresholding, and overlapping signals were separated via watershed segmentation. The "Analyze Particles" tool in ImageJ was then used to count individual *Mid1* mRNA molecules (each fluorescent particle representing one transcript).

GSK3685032 treatment

Mouse fibroblasts were cultured under standard conditions and treated for 4 days with either vehicle control or 1 μM GSK3685032. Vehicle-treated cells received an equivalent volume of DMSO. Three biological replicates were included for each condition. Following treatment, fibroblasts were sent to Plasmidsaurus for bulk RNA sequencing, and genomic DNA was collected using Qiagen DNeasy Blood & Tissue Kit (Qiagen#69504). *Mid1* gene expression was quantified as counts per million (CPM) and compared between vehicle- and GSK3685032-treated samples. For DNA methylation analysis, genomic DNA was bisulfite converted using the Zymo EZ DNA Methylation-Gold Kit (Zymo#D5006). Regions of interest within *Mid1*, including DMR2, DMR4, DMR5 upstream, and DMR5 downstream, were PCR amplified from bisulfite-converted DNA and sequenced by Oxford nanopore sequencing. Reads

were aligned to mm10 reference genome and methylation levels were quantified using Bismark. Percent methylation was calculated for each CpG site and compared between vehicle- and GSK3685032-treated samples.

QUANTIFICATION AND STATISTICAL ANALYSIS

Mice were assigned to experimental groups based on genotype and treatment conditions, with littermates distributed across cohorts and processing batches in parallel to balance cage, litter, and batch effects. Blinding was tailored to each modality. Freezing behavior was scored by automated tracking system FreezeFrame 5 that was intrinsically blinded to group assignment. Histological cell counts were generated by machine-learning–based automated pipelines, with the analyzing experimenter receiving only coded animal identifiers. WGBS and PIP-seq libraries were prepared in parallel using commercial and identical protocols and tracked by numeric IDs. Library identity was re-associated only at the statistical comparison step. All computational analyses ran on coded sample-level inputs through standard, deterministic pipelines. Stereotaxic viral injections were the only procedure not blinded to viral identity, as accurate delivery required ID tracking. All downstream readouts from these animals were nonetheless acquired and analyzed under the blinded conditions above. Animals with off-target injections or absent transgene expressions were excluded based on post hoc histology. Statistical comparisons used two-tailed Student's T-tests or two-way ANOVA with appropriate post hoc tests, as specified in figure legends along with sample sizes (n), the unit of replication, and exact p values. Data are presented as mean ± SEM unless otherwise indicated.